The frost heave characteristics of a volcanic coarse-grained soil quantified by particle image velocimetry

Junping Ren[1*], Shoulong Zhang[2], Tatsuya Ishikawa[2], Shuangyang Li[3], Chong Wang[1]

[1] MOE Key Laboratory of Mechanics on Disaster and Environment in Western China, College of Civil Engineering and Mechanics, Lanzhou University, Lanzhou 730000, China

[2] Division of Field Engineering for the Environment, Hokkaido University, Sapporo 060-8628, Japan

[3] State Key Laboratory of Frozen Soil Engineering, Northwest Institute of Eco-Environment and Resources, Chinese Academy of Sciences, Lanzhou 730000, China

*Corresponding author: Junping Ren

Email: renjp@lzu.edu.cn

Abstract

The increasing use of the seasonally frozen and permafrost regions for civil engineering constructions and the effects of global warming on these regions have stimulated research on the behaviors of frozen soils. In the present study, the frost heave characteristics of a coarse-grained soil with volcanic nature was experimentally investigated. A large soil tank model was established in laboratory for this purpose. The effects of temperature boundary, external water supply, and water transfer type on the frost heave characteristics of the volcanic soil were studied, through a series of frost heave tests. The particle image velocimetry (PIV) technique was used to quantify the full field deformation of the soil specimen. The results suggest that temperature gradient inside the soil specimen is the driving force for the migration of pore water and vapor. The largest increment in water content generally agrees well with the frost penetration depth. The contribution of vapor to the frost heave of the Komaoka soil specimen is typically small. The applied seeding method, selected subset size, image-object space calibration, and calculation processes ensured accurate PIV results. Discussions regarding the presented experimental investigation and the employment of PIV technique for quantifying frozen soil deformation are summarized. These findings and discussions can provide valuable insights into the frost heave behavior of the studied soil in particular, as well as promote the application of PIV for frozen soil engineering.

Keywords: *Frozen soils, frost heave, water transfer, PIV, full field deformation*

1. Introduction

Nearly one-third of the land surface of the Earth experiences freezing and thawing annually (Lu et al., 2021). The increasing use of the seasonally frozen and permafrost regions for such as civil engineering constructions and the effects of global warming on these regions have stimulated research on the behaviors of frozen soils (Gao et al., 2020; He et al., 2021; Rempel, 2010; Saberi and Meschke, 2021). Among the behaviors of frozen soils, frost heave is an important aspect, which is typically induced by water migration in the soil mass during freezing, under the temperature or cryogenic suction gradient. The importance of frost heave has been seen in agronomy, geography, and engineering for decades (e.g., Konrad, 1988; Peppin and Style, 2012; Smith, 1985; Sweidan et al., 2022; Watanabe, 1999).

The formation of rhythmic lenses of ice in freezing soils is an intriguing geo-physical phenomenon that is not fully understood, despite much experimental and theoretical work over the past century (Peppin and Style, 2012). Whilst it is true that certain soils are more frost susceptible than others, frost heave is not an intrinsic soil property, but rather the result of the combined thermal, hydrologic, and stress conditions in the soil (Smith, 1985). In general, three conditions need to be satisfied for the formation of ice lenses and the occurrence of frost heave: frost susceptible soil, sufficiently cold temperature to cause soil freezing, and external water supply (Zhou et al., 2014). Due to their weak water retention capacity, coarse-grained soils are typically considered as non-frost susceptible in engineering practice. However, recent researches have shown the importance and contribution of vapor transfer to ice accumulation or frost heave in relatively dry coarse-grained soils, through experimental studies and numerical modeling (e.g., Teng et al., 2019; Wang et al., 2019; Zhang et al., 2016).

Measurement of soil deformation using particle image velocimetry (PIV) technique (aka digital image correlation (DIC)) has become routine experimental practice in many geotechnical research laboratories over the past two decades (e.g., Bhandari et al., 2012; Liu et al., 2011; Nishimura et al., 2016; Stanier and White, 2013; Stanier et al., 2016a, b; Viggiani and Hall, 2012; Xu et al., 2021, 2022). The PIV/DIC is essentially a mathematical tool for assessing the spatial transformation (including translations and distortions) between two digital images. There are some commercially and freely available PIV/DIC software used for geotechnical analyses. For example, the GeoPIV-RG is a Matlab module which implements PIV for

quantifying the deformation in soils (e.g., White et al., 2003; Take, 2015). A flowchart for GeoPIV-RG computations is provided by Stanier et al. (2016a). The accuracy of the PIV system depends on the optics of the image formation, the image processing algorithm, and the image to object space transformation determined by the camera calibration (White et al., 2005). In recent years, there has also seen the combination of PIV and machine learning techniques. For example, Gao et al. (2021) proposed a new velocity field estimation paradigm, which is a synergetic combination of cross correlation and fully convolutional neural network. The proposed deep learning model embedded with cross correlation can suppress noise and obtain satisfying results for practical applications.

In spite that PIV has been widely used to quantify the full field deformation of unfrozen soils, its use in the frozen soil area is rather limited (e.g., Dagli et al., 2018; Liu et al., 2018; McKnight-Whitford, 2013; Nishimura et al., 2021; Wang et al., 2020; Zeinali et al., 2020). Arenson et al. (2007) and Azmatch et al. (2008) investigated ice lens growth and soil strain development during freezing by using GeoPIV, which is an old and less precise version of the GeoPIV-RG. The occurrence of ice lenses in the soil body may cause difficulties in using PIV to analyze frost heave. For example, the ice lenses show low spatial variation in brightness, which means that their texture is not sufficient for accurate calculation. Arenson et al. (2007) concluded that a new ice lens will change the patch characteristics (due to the separation of soil body by ice lensing) so that PIV is no longer able to trace the patch. Wang et al. (2020) conducted a parametric study on the selection of tracer particles, which may be necessary to the PIV analysis on freezing fine-grained soils, as the image textures of fine-grained soils may not be clear enough. One common limitation of these studies is that a sound image to object space transformation was not established. They instead used a constant conversion factor to determine the frost heave of the soil specimen from the measured pixel values (e.g., Dagli et al., 2018; Wang et al., 2020).

The present study aims to investigate the frost heave characteristics of a volcanic coarse-grained soil, which was sampled from the southern district of the Sapporo city, Hokkaido, Japan. A relatively large soil tank model was established in laboratory for this purpose. Eight tests in total were carried out to study the effects of temperature boundary, external water supply, and water transfer type on the frost heave characteristics of the volcanic soil. Experimental details

such as the temperature and moisture distributions, and frost heave development in the soil specimen were obtained and analyzed. In addition to the frost heave measured by a displacement sensor, the PIV technique was used to quantify the full field deformation of the soil specimen. Details regarding the setup of the PIV technique such as seeding method, selection of proper subset size, and image-object space transformation are provided. Discussions with respect to the presented experimental investigation and the employment of PIV technique for quantifying frozen soil deformation are summarized. The results of the present study can provide valuable insights into the frost heave behavior of the studied soil in particular, as well as into the application of PIV for frozen soil engineering in general.

2. Experimental setup

2.1 Experimental material

Volcanic soils cover 1% of the Earth's surface (Neall, 2009). One of the major areas of volcanic soils rim the Pacific and occur in countries such as Japan. In the Hokkaido prefecture of Japan, there are over 40 Quaternary volcanoes, and pyroclastic materials (e.g., volcanic ash, pumice, and scoria) cover over 40% of these areas (Kawamura and Miura, 2013). The volcanic soils have been considered problematic since they show different behavior from that of clay or sand. The focus of the present study is on the frost heave characteristics of the Komaoka soil, which is a typical volcanic soil found in Hokkaido. The original soil was sampled from the ejectas of the Shikotsu calderas near the Sapporo city, as shown in Fig. 1.

The Komaoka soil contains a considerable amount of highly porous particles, and owns a low in-situ dry density (i.e., 0.794g/cm^3 (Nguyen, 2017)). In the present study, the soil particles with sizes smaller than 2mm were used for the frost heave model test, which will be described in the next section. The basic properties of the Komaoka soil are summarized in Table 1, and its gradation curve is shown in Fig. 2. The Komaoka soil has a very low fraction of clay (i.e., 8% by weight) and is classified as a non-plastic coarse-grained soil. The soil freezing characteristic curve (SFCC) of the Komaoka soil subject to various testing conditions has been investigated by the authors (Ren et al., 2021).

2.2 Frost heave model test

In the present study, a relatively large soil tank with the dimension of 550mm(L)*150mm(W)*400mm(D) was used to investigate the frost heave characteristics of the Komaoka soil. Figure 3 is a photo that summarizes the components and setup of the frost heave test. A schematic diagram with labeled dimensions and details of the frost heave model test is also shown for better illustration (see Fig. 4). The main steps for conducting the frost heave test are summarized below.

A certain amount of oven-dry Komaoka soil (< 2mm) was mixed with distilled water and left for more than 24h for achieving uniform moisture distribution. The prepared wet Komaoka soil, with the desired gravimetric water content (e.g., 30%), was compacted layer by layer in the soil tank to the target dry density (i.e., 0.915g/cm^3). The thickness of each layer was approximately 30mm and the total thickness of the compacted soil specimen was generally around 265mm. During the compaction process, 12 EC-5 moisture sensors and 12 T-type thermocouples were installed at desired locations (as shown in Figs. 3 and 4), through the 16 sensor holes (four rows with four holes on each row) that are available on the back acrylic wall of the soil tank. The moisture and temperature sensors were calibrated prior to their use. The calibration procedures were similar to those summarized in Ren et al. (2021). These sensors were connected to a data logging system (see Fig. 3). The data logging time interval was generally 5min during the frost heave test.

After compaction and sensor installation, the top plate was placed on the top surface of the soil specimen (see Fig. 4(b)). To minimize friction, silicone grease was smeared on the four sides of the top plate before installing it. The silicon grease and O-ring encircling the top plate contributed to sealing the gaps between the top plate and the acrylic wall, preventing any moisture loss during the experimental process. The temperatures of the top and bottom plates (e.g., -10 and +20°C, respectively) were controlled by two low-temperature baths. The temperature gradient in the soil specimen facilitated the migration of liquid and/or vapor to the freezing front. Constant temperature boundary (i.e., 5°C, which was the ambient temperature controlled in the environmental chamber (with the dimension of 2.9m(L)*2.85m(W)*2.4m(H)) where the whole setup was located) was exerted on the four side surfaces of the soil tank. The freezing process was followed by fast thawing, during which the temperature of the top plate

was adjusted to 25°C while the bottom temperature was maintained unchanged. In addition, the environmental chamber was allowed to recover to room temperature (around 22°C) during the thawing process, facilitating fast thawing of the soil specimen.

A linear variable differential transformer (LVDT) was installed on the top plate to measure the vertical deformation of the soil specimen during the freezing and thawing processes. To facilitate the development of frost heave, external water can be supplied to the soil specimen via a Mariotte bottle, which applies constant water pressure on the specimen's bottom surface. Overburden pressures can be exerted on the soil specimen, if necessary. After the frost heave test, the top plate was removed and the soil specimen was examined for water redistribution. A couple of soil samples at different locations along the height of the specimen were collected to determine their total water contents, by oven dry method. This facilitates the analysis of the contribution of liquid and vapor transfer to water distribution in the soil specimen during the freezing process.

A total of eight frost heave tests (Test 1 to Test 8) were carried out in the present study. Two weeks were typically required for one single test. In general, the soil specimen was preconditioned for 24h for achieving uniform temperature and moisture distribution before starting testing. As summarized in Table 2, the soil specimens were tested under different initial water contents and freezing/thawing temperatures, and the availability of external water supply. In particular, in order to investigate the effect of vapor transfer on the frost heave characteristics of the Komaoka soil, four of the eight tests (i.e., Test 4, 6-8) incorporated a layer of dry coarse particles (approximately 75mm thick), above which the wet Komaoka soil (< 2mm) was compacted (approximately 190mm thick). The coarse particles layer was aimed to separate the external water at the bottom of the soil tank from the upper Komaoka soil. The material used for this layer was coarser Komaoka soil particles (with sizes between 2.8-9.5mm) in Test 4, and glass beads (mostly between 2 to 4mm) in Tests 6, 7, and 8.

However, during Test 4, it was found that the capillary rise was relatively high and the coarser Komaoka soil particles became wet. As a result, both liquid and vapor transfer might have occurred during the freezing process in Test 4. On the contrary, there was basically no capillary rise in the glass beads layer in Tests 6, 7, and 8. Therefore, it can be reasonably assumed that only vapor can flow into the Komaoka soil during freezing (under temperature

and vapor pressure gradients), from the water reservoir and through the boundary between the glass beads layer and the Komaoka soil layer. In addition, the Komaoka soil specimen in Tests 7 and 8 had an initial gravimetric water content of 7%, which corresponds to a volumetric water content of 0.064 m^3/m^3. This value can be approximately taken as the residual water content of the Komaoka soil, according to Ren et al. (2021). Therefore, it can be assumed that only vapor transfer existed in the soil specimen of Tests 7 and 8.

2.3 Quantification of soil deformation by PIV

During the frost heave test, a LVDT was used to measure the overall deformation of the soil specimen. This deformation only represents the vertical displacement of the top surface of the soil specimen. On the other hand, the PIV technique can be used to quantify full field deformation of the soil specimen. In the present study, a Panasonic digital camera, DMC-TX1, with 4864 pixels in length and 3648 pixels in width, was used to automatically capture images of the front surface of the soil specimen during the testing period (as shown in Fig. 3). The thickness of the acrylic wall of the soil tank is around 38mm. This is assumed to have insignificant influence on the PIV deformation computation (e.g., White et al., 2001). The time interval for imaging should be small, which can ensure high correlation between consecutive image pairs. The imaging interval was generally 3min in the present study. The obtained images were used to analyze the deformation field of the soil specimen by using GeoPIV-RG.

It is generally considered that coarse-grained soils such as natural sand has its own texture in the form of different colored grains, and the light and shadow formed between adjacent grains when illuminated. The Komaoka soil (< 2mm) is classified as a non-plastic coarse-grained soil as it contains 64% sandy particles. Therefore, the soil texture of the front surface may be adequate for fulfilling a sound PIV calculation. Two of the eight tests (Tests 1 and 2) were conducted under this situation (i.e., without seeding the front surface of the soil specimen). However, it was found that the image intensity contrast was relatively low (see Fig. 5), which could not guarantee an accurate calculation result. Therefore, seeding the front surface of the soil specimen was necessary for achieving good image quality.

In the present study, the seeding particles used were the coarser Komaoka soil particles that are with sizes from 2.0 to 2.8mm. This was aimed to introduce as little disturbance as possible

to the Komaoka soil specimen used for frost heave test. The seeding particles were added only to the front side of the soil specimen (the adding procedure was similar to that described in Liu et al. (2018) and Wang et al. (2020)), such that the seeding particles did not significantly affect the frost heave characteristics of the soil specimen. Although the seeding particles were not homogeneously distributed across the front surface of the soil specimen in the present study, it was adequate for providing sufficient intensity contrast (as will be shown below), ensuring a reasonable calculation by PIV. The comparison between seeding and without seeding the front surface of the soil specimen is summarized in Fig. 5. Tests 2 and 5 were selected for comparison, and a subset with the size of 150*150 pixels was generated on each of the images obtained from the two tests. It can be seen that the standard deviation of the subset pixel intensities (i.e., Std(I_s)) and the sum of squares of subset pixel intensity gradients (SSSIG) for Test 5 are much higher than those for Test 2, suggesting that seeding the front surface resulted in sufficient intensity contrast, based on which good correlation calculation can be achieved.

The precise alignment of the camera and front surface of the soil specimen is necessary for a good computation result. The light provided by the two LED lights in the environmental chamber was sufficiently bright and uniform for capturing high quality images. Another important aspect of the PIV technique is to set up control points, which can provide accurate displacement calculation. Therefore, a total of 21 control points were set up for the image-object coordinate calibration in the present study. The control points were distributed uniformly throughout the region of interest (as an example, see Fig. 6), to ensure that the deduced calibration parameters represent a good fit for the entire image. However, a detailed description of the setup process for these control points is absent the scope of the present study. Interesting readers can refer to the study by Take (2015).

3. The accuracy of PIV for frost heave quantification

The purpose of this section is to determine an optimum subset size, which can ensure accurate displacement calculation and mitigate computational burden at the same time. The optimum subset size is then used to calculate the deformation field of the soil specimen for all the eight frost heave tests. The images and experimental results of Test 5 were selected for illustration. For the PIV calculation in the present study, the shape of the subset was square, and

six different subset sizes were chosen for comparison. They were, 50, 75, 100, 150, 200 and 250 pixels, respectively.

Figure 6 is an example showing the front surface of the soil specimen and some portions of the test equipment, such as the top and bottom plates. The dimension of this image is 4864*3648 pixels. The same calculation area was selected when investigating the effects of subset size on the number of subsets generated in this calculation area (see Fig. 7), and on the intensity contrast of the subsets (see Fig. 8). It can be seen from Fig. 7 that when the subset size is 150 pixels, the number of subsets is 434. However, when the subset size is set to 50 pixels, the number of subset approaches to 3811. This suggests that larger subset size can significantly mitigate the computational burden, as thousands of images are generally taken (and need to be processed sequentially) for one single frost heave test.

Figure 8 shows the effect of subset size on the intensity contrast of the generated subsets, that is, Std(I_s) and SSSIG. Stanier et al. (2016b) summarized that the Std(I_s) should be greater than 15 so as to ensure that there is sufficient contrast within the subsets. In addition, the SSSIG provides another measure of subset quality with a minimum threshold of $1*10^5$ for precise calculation. These two threshold values are plotted in Fig. 8 for better comparison. It can be seen that larger subset size generally yields larger Std(I_s), and the SSSIG increases significantly with the increase of the subset size. For the subset size larger than 150 pixels, the SSSIG of the subsets basically locates above the suggested threshold value.

In spite that smaller subset size can be used to better define local displacement of the soil specimen, it generally results in low intensity contrast, leading to low correlation coefficient between image pairs and therefore low accuracy. On the contrary, larger subset size can result in higher correlation coefficient although the displacement field loses some details. For the trade-off between computational burden and displacement field resolution, the optimum subset size was chosen as 150 pixels in the present study.

Further validation of using the subset size of 150 pixels for displacement field calculation is illustrated in Fig. 9. This figure compares the vertical displacement of the soil specimen surface calculated by PIV with the subset size of 150 pixels and that measured by LVDT, for Test 5. It can be seen that at the selected time steps, the vertical displacement of the soil specimen surface calculated by PIV has good agreement with its measured counterpart,

although the former is slightly less than the latter. The difference between the two displacement curves is computed and plotted in the same figure. It shows that the difference between the two curves increases in the first 10h after the frost heave test started. After that, their difference does not change significantly and stabilizes in the range of 0.3mm to 0.35mm with slight variation. The reason for this difference may come from the fact that the centers of the generated subsets of the top row did not exactly locate on the top surface of the soil specimen, which were approximately 6.5mm below the top surface, as shown in Fig. 6. As a result, the amount of frost heave difference (i.e., roughly 0.35mm after 10h) might mainly occurred in the soil body between the soil specimen surface and the subset centers of the top row. Once there was no further frost heave in this portion of soil body, it would move upward as a rigid body, resulting in a relatively stable difference about 0.3mm afterwards. Therefore, the soil deformation calculated by PIV can be considered reasonable.

4. Experimental results and analysis

4.1 General results of the frost heave test

As mentioned above, a total of eight frost heave tests were carried out in this study. A variety of factors that influence the frost heave characteristics of the Komaoka soil was considered when designing those tests. The influencing factors include such as soil initial water content, freezing and thawing temperatures, external water supply, and the way of water transfer (i.e., liquid or vapor, or both). Test 5 is selected as an example to show the general results obtained from these frost heave tests.

Figure 10(a) shows the measured temperature by four thermocouples in the soil specimen during the freezing process of Test 5. The four thermocouples were located on the same vertical section but four different rows (they were labelled as T1, T4, T7, and T10, respectively) as illustrated in Fig. 4. It can be seen that the variation trends of temperature at different depths along the same vertical section are similar. The soil temperature decreases fast during the initial freezing stage, and its rate of decrease reduces with the elapsed time. After about 60h, the temperature at these depths becomes relatively stable. The freezing process was typically maintained for over 7d. The fluctuation of the temperature curve was caused by the variation of the ambient temperature of the large environmental chamber, as a result of temperature

310 regulation process. However, this fluctuation is not considered to have significant effect on the
311 frost heave characteristics of the soil specimen, as a smooth frost heave curve was obtained.
312 The measured volumetric water content by four EC-5 sensors at four positions during the
313 freezing process is summarized in Fig. 10(b). Similarly, the four EC-5 sensors were on the same
314 vertical section but different rows. The initial volumetric water content measured by EC-5 was
315 around 0.27m^3/m^3, which is reasonable (the initial gravimetric water content was 30% and the
316 soil dry density was 0.915g/cm^3). The M3 was located on the first row, therefore, the volumetric
317 water content measured by M3 decreases significantly during the initial freezing stage. This
318 shows that the soil mass close to the cold top plate was frozen rapidly. Compared to M3 and
319 M6, M9 and M12 were much closer to the warm bottom plate, where external water was
320 supplied. As a result, the water content measured at these two locations show overall increase.
321 M6 was located between M3 and M9. Although its value influenced by water supply, it shows
322 significant reduction in water content, due to water migration upwards as well as the penetration
323 of the freezing front. It needs to be mentioned that the unusual change in the measured
324 volumetric water content by M6, M9 and M12 is attributed to the nonideal control of water flux
325 during external water supply.
326 The frost heave development measured by LVDT is shown in Fig. 10(c). It can be seen that
327 the amount of frost heave increases dramatically in the initial freezing period. After 40h, the
328 rate of frost heave decreases, but the soil surface still deforms upwards. The final frost heave
329 achieved in this test is approximately 7.4mm. In addition, no apparent ice lenses were observed
330 during the freezing process. Figure 10(d) summarizes the comparison between the initial and
331 final (after thawing) gravimetric water content distribution along the depth of the soil specimen.
332 Thawing of the specimen was purposely controlled to be fast, therefore, water redistribution
333 during the thawing process was neglected. It clearly shows that the water content of the soil
334 specimen increases significantly during the freezing period. In addition, the largest increment
335 in the water content occurs around a depth of 10cm from the top of the soil specimen. This
336 value is in agreement with the frost penetration depth, which approached to a depth of 10cm
337 after 40h and then slowly penetrated downward (as shown in Fig. 10(c)). This suggests that
338 liquid water in the soil specimen had enough time to accumulate in this narrow range, towards
339 where water migration was significant.

Figure 11 shows the calculated vectorial displacements and vertical displacement contours by PIV when the soil specimen achieved the maximum frost heave value in Test 5. The frost penetration depth is also shown in this figure for better illustration. It can be seen from the vectorial plot that soil surface has the largest deformation, and the deformation decreases with the increase of soil depth. In the vertical displacement contours (i.e., Fig. 11(b)), the negative sign for the color bar means expansion (i.e., frost heave). It can be known that frost heave is relatively uniform across the soil specimen horizontally, and the bottom part of the soil specimen barely deforms (neither compressed nor expanded). This is reasonable since the soil body below the frost penetration depth kept unfrozen, and no impact from the phase change of pore water is expected.

The summary of the vertical displacements for the subsets on each row (see Fig. 6) is depicted in Fig. 12. The subset row was numbered from top down. Smaller row number means that the subsets were located on the upper part of the soil specimen image. It can be seen that the deformation of the upper subsets is approximately linearly distributed, while those at the bottom part of the soil specimen barely deform. A linear equation can be best-fitted to the average value of the vertical displacement of the subsets on each row, with a coefficient of determination of 0.99.

A series of vertical displacement contours at different times can be plotted to show the frost heave development during the freezing process, as shown in Fig. 13. The frost penetration depth and frost heave at each selected time are also indicated. Note that the frost heave value on each subplot was measured by LVDT, which is close to yet slightly larger than its calculated counterpart by the PIV technique (see the color bar of each subplot), as explained in the previous section. It can be seen that with the gradual penetration of the freezing front, the frost heave of the soil specimen becomes larger. The frost heave is relatively uniform across the soil specimen during the freezing process. However, there is also some nonuniformity near the two side boundaries, possibly caused by the friction between the soil specimen and the acrylic wall, as well as the side temperature boundary condition.

When the soil specimen was thawed and settled, it was found that the top plate was not able to move downward freely, due to the friction between the top plate and the acrylic wall. As a result, there was a gap between the top plate and the surface of the thawed specimen, as shown

in Fig. 14. In this scenario, the PIV method is particularly useful for quantifying the thaw settlement of the soil specimen, as the LVDT was stuck by the top plate. Figure 15 shows the computed vertical displacement of the soil specimen by PIV. The positive numbers along the color bar indicate compression. It can be seen that the thaw settlement is around 3.5mm, which is smaller than the frost heave achieved during the freezing process (i.e., 7.4mm). This suggests that soil particles were not fully recovered to their original locations, and there was plastic deformation in the soil specimen. In addition, the thaw settlement of the soil specimen shows relative uniformity and linear distribution, with the bottom part barely deformed, similar to the frost heave case shown in Fig. 11.

4.2 Effect of temperature boundary

The effect of temperature boundary condition on the frost heave characteristics of the Komaoka soil is investigated in this section, through the comparisons between Test 1 and Test 3, which were carried out under closed-system condition, and between Test 7 and Test 8, which were tested under vapor transfer condition.

The temperature distribution curves of Test 3 at different time steps during the freezing period are shown in Fig. 16(a). The measured temperature values of the four locations that were approximately in the middle section of the soil specimen (i.e., T2, T5, T8, and T11 in Fig. 4) were used, along with the top and bottom plate temperatures. It can be seen from this subfigure that the temperature distribution along the depth of the soil specimen is nonlinear in the early period of freezing. However, with time elapsing, the temperature distribution curve gradually becomes linear. After about 48h, the temperature distribution along the soil specimen is basically stabilized, indicating the establishment of thermal equilibrium (i.e., steady state) in the soil specimen.

The frost penetration depth can be determined by identifying the 0 ºC location (i.e., freezing front) at different times through Fig. 16(a). Figure 16(b) summarizes the graphically determined frost penetration depth and the frost heave measured by LVDT in Tests 1 and 3. It shows that the maximum frost heave value of Test 3 is larger than that of Test 1, which approach to 5.9mm and 4.2mm, respectively. This is related to the frost penetration depths of the two tests. In Test 3, the frost penetration depth was deeper. As a result, more portion of the soil specimen was

subject to freezing, and more water were likely to migrate upward and change phase to ice. Although both these two tests were tested under closed-system condition, the initial high-water content of 30% could facilitate the migration of pore water upward to the freezing front. In addition, the frost heave still showed a sign of increase when the tests were stopped.

For Tests 7 and 8, different temperature values were imposed on the top and bottom surfaces of the soil specimen. However, the temperature difference between the top and bottom plates in these two tests was the same. This means that the two tests had the same temperature gradient during freezing (i.e., approximately 0.113ºC/mm). It can be seen from Fig. 17(a) that Test 8 yields much deeper frost penetration since colder temperature was imposed on the top surface of the soil specimen. On the other hand, the variation in the frost heave curves of these two tests are basically the same. The frost heave achieves a value around 0.45mm after only 10h since the start of freezing, and then barely changes with the rest of the freezing process. The reason for this very limited frost heave is that the soil specimens in these two tests had very low initial water content (i.e., 7%), and external water was supplied in the form of vapor. As a result, the amount of water transferred to the soil specimen in these two tests was limited.

Figure 17(b) summarizes the water distribution along the soil specimen before freezing and after thawing for the two tests. The contribution of vapor to the frost heave of the soil specimen is hard to be quantified in this case. On one hand, most of the frost heave occurred in the first 10h in these two tests. Therefore, the observed frost heave should mainly due to pore water freezing in the upper portion of the soil specimen. On the other hand, the incremental area of the water distribution curve is larger than the decremental area, which could be the evidence that vapor from the water reservoir went into the soil body. Although Test 8 assumes higher water content than Test 7 does, this does not contribute to significant frost heave, since the heave difference between the two tests can be barely distinguished. This implies that vapor transferred to the freezing front and changed phased to ice locally, without affecting the original pore structure of the soil specimen. In addition, the water content of the upper part of the soil specimen in Test 7 is larger than its counterpart in Test 8, suggesting that slower frost penetration results in grater water migration and accumulation. The location of the maximum water content corresponds well to the frost penetration depth in these two tests.

4.3 Effect of external water supply

The comparison between the results of Test 3 and Test 5 is summarized in Fig. 18. In these two tests, the initial water content of the soil specimen and temperature boundary conditions were the same. However, Test 3 was carried out under closed-system condition, while external water was supplied to the soil specimen in Test 5. Figure 18(a) shows the frost penetration depth and frost heave of the two tests. The frost penetration depth is determined from the temperature distribution curves at different times. It can be seen that the frost penetration depth of the two tests show similar evolution trend. On the other hand, the frost penetration depth in Test 3 is deeper than in Test 5. This difference may be because that significant amount of external water was supplied to the soil specimen in Test 5. As a result, the latent heat released by the excess water contributed to counterpart the cold energy imposed by the top plate, resulting in a relatively lower penetration depth.

In the early period of freezing (i.e., within 5h since the start of freezing), the frost heave curves of the two soil specimens show similar evolution trend and insignificant difference. This is reasonable since the two soil specimens had the same initial water content and were subject to the same temperature boundary conditions. In spite that external water was supplied at the bottom of the specimen in Test 5, it can be assumed that external water was not yet able to migrate to the upper part of the specimen. As a result, the frost heave occurred within this short period of time was mainly from the migration of water that were originally in the upper portion of the soil specimen, similar in the two testing scenarios. Both the two specimens show relatively large frost heave rate during this period. However, as time elapses, large difference between the two frost heave curves occur, which can be attributed to the different external water supply conditions. The maximum frost heave achieved in Test 3 is about 6.0mm, while that in Test 5 approaches to 7.4mm. The frost heave rate is less than that in the early freezing period, but it still shows trend of increase at the end of the freezing process.

Figure 18(b) shows the change of water distribution in the two soil specimens. It can be seen that there is significant difference between the final water content profiles of the two specimens that were subject to the same freezing condition. In Test 3, the water content of the upper portion of the soil specimen increases, while the bottom part shows decrease in water content. This observation is reasonable since pore water should have migrated from the lower

460 portion of the soil body to its upper portion, due to temperature (cryogenic suction) gradient.
461 The maximum increment in the water content in Test 3 occurs at a depth about 12cm, which
462 shows agreement with the frost penetration depth, considering the depth interval (around 2.5cm)
463 for determining water content along the soil specimen. On the other hand, the final water
464 content values at each tested location along the soil specimen in Test 5 show significant increase,
465 compared with their original values before freezing (i.e., 30%). In addition, the final water
466 content achieved in Test 5 is much larger than that in Test 3. For example, the maximum water
467 content after thawing in Test 5 is around 58%, while that in Test 3 is only 36%. In Test 5, the
468 water content of the lower portion soil mass owns larger increment, compared with its upper
469 counterpart. This is because external water was supplied to the bottom surface of the soil
470 specimen, which then migrated upward. The maximum water content after thawing in Test 5
471 occurs at a depth of 10cm, which is coincident with the frost penetration depth in this test.
472
473 **4.4 Effect of water transfer type**
474 Figures 19 and 20 summarize the comparison between the experimental results of Test 5
475 and Test 8, where liquid and vapor transfer were considered to be the main type of water transfer
476 respectively. It can be seen from Fig. 19 that at the early stage of freezing (e.g., within 25h after
477 starting the test), the frost penetration rate in Test 8 is larger than that in Test 5. In Test 8, the
478 frost penetration depth approaches to lower than 12cm after 25h, while it is only about 8cm in
479 Test 5. After that, the frost penetration rate in Test 8 significantly decreases and the freezing
480 front stabilizes at a depth about 13cm. On the other hand, the frost penetration rate in Test 5
481 decreases gentler and a final frost depth close to that in Test 8 is achieved. The difference
482 between the frost penetration curves of the two tests can be attributed to their different initial
483 water contents and temperature boundary conditions.
484 The maximum frost heave values measured in Test 5 and Test 8 are 7.4 and 0.5mm,
485 respectively. The reason for this significant difference is that in Test 5, external water was
486 continuously supplied to the bottom of the soil specimen, which facilitated liquid water
487 migration to the freezing front, and therefore resulting in significant frost heave. However, in
488 Test 8, the glass beads layer prevented any liquid water from migrating to the soil specimen
489 since there was basically no capillary rise in the glass beads. Instead, it is suggested that vapor

was transferred to the soil specimen through its boundary with the glass beads layer, due to temperature and vapor pressure gradients. It should also be noted that ice lenses were not observed in neither of the two testing scenarios.

Figure 20 shows the initial and final water contents of the two soil specimens. This further supports the above conclusions. It can be seen that in Test 5, there is significant increase in water content along the depth of the soil specimen. The increased water was externally supplied, as explained previously. In Test 8, soil specimen above the glass beads layer shows some increase in water content. The increased water was mainly from vapor transfer through the boundary between the soil specimen and the glass beads layer. The water content of the lower part of the soil specimen changed from 7% to 6%, i.e., a slight change. Therefore, the relatively large increment of water content at the freezing front should be mainly due to vapor transfer.

In addition, for all the four tests conducted under vapor transfer condition (i.e., Tests 4, 6, 7, and 8), very small amount of frost heave (i.e., less than 0.5mm) were observed. This suggests that vapor transfer only contributed to very limited frost heave of the soil specimen, under the testing conditions in the present study.

5. Discussion

The problems with respect to many frost heave tests carried out in laboratory are that: (1) the soil specimen is small (such that the installation of moisture and temperature sensors will significantly affect the properties of the soil specimen), (2) the rate of freezing is typically high (large temperature gradient), and (3) the testing time is relatively short (e.g., a few days) (Williams and Smith, 1989). These testing conditions deviate from in-situ case which generally involves large soil mass, small temperature gradient and long freezing time. In the present study, a relatively large soil tank model was employed to investigate the frost heave characteristics of the Komaoka soil. In addition, a relatively small temperature gradient (i.e., ~0.113ºC/mm) was imposed on the soil specimen, and each of the eight tests lasted till the steady state was well established. Therefore, the testing conditions of the present study should be more representative to in-situ freezing conditions.

The Komaoka soil used was classified as a coarse-grained soil with a small fraction of clayey particles. Various testing conditions were exerted on the large soil specimen and the

effects of temperature boundary condition, the availability of external water supply, and the type of water transfer on the frost heave behavior of the soil were studied. This experimental program is relatively time- and labor-consuming. The analysis on the frost heave characteristics of the Komaoka soil indicates that lower temperature of the cold plate typically leads to deeper frost penetration. The temperature gradient inside the soil specimen is the driving force for the migration of pore water and vapor. The largest increment in the water content generally agrees well with the frost penetration depth. When the initial water content of the soil specimen is high, large amount of pore water is available and liquid water migration is the main type of water transfer for the development of frost heave. As a result, large frost heave was observed regardless of the availability of external water supply (e.g., Tests 1, 3, and 5), though ice lenses did not apparently develop. However, when there is mainly vapor transfer in the soil specimen, the frost heave is very limited. This suggests that the transferred vapor from the water reservoir changed phase locally in the pore space, where only a small amount of water exists, as the soil specimen has low initial water content (e.g., Tests 6, 7, and 8). The above observations are consistent with other studies on soil frost heave behavior (e.g., Yin et al., 2018).

One limitation of the present study, however, is that external water supply was not ideally controlled. And, the volume of water absorbed by the soil specimen was manually read from the scale on the Mariotte bottle. Therefore, the water flux was not perfectly recorded. In addition, the effect of overburden pressure on the frost heave of the Komaoka soil was not considered. However, overburden pressure will generally lead to less extent of frost heave, according to the literature (e.g., Yin et al., 2018).

The advantage of using PIV is that it can quantify the deformation field of the soil specimen, rather than only knowing the deformation of the top surface as measured by LVDT. There are a number of factors that affect the accuracy of PIV calculation on soil deformation. They include such as lighting condition, textural features of the soil, image quality, subset size, evaluation methods, and image-object space calibration method. In the present study, the calculated deformation of the top surface of the soil specimen shows relatively small difference to that measured by LVDT, indicating that the seeding method, selected subset size, image-object space calibration, and computation processes are reasonable and accurate. Therefore, the setup of control points is highly recommended, instead of using a constant conversion coefficient for

550 the transformation from pixel coordinates to object-space coordinates.

551 It is possible to select a narrow area of the front surface and calculate its deformation field.
552 However, the present study aimed to investigate the full field displacement of the front surface,
553 which can give the overall deformation information of the soil specimen. For example, the
554 boundary effect is observed from the contour plots of vertical displacement (see Fig. 13). The
555 boundary effect shows that there is likely some friction between the soil mass and the acrylic
556 wall of the soil tank. On the other hand, the large size of the soil tank as well as the specimen
557 ensured a uniform deformation of the soil mass which is away from the acrylic walls, resulting
558 in good accuracy.

559 When employing the PIV technique on freezing soils, a few factors may affect the image
560 quality of the soil specimen. For example, the color of the soil specimen may change during the
561 freeze and thaw processes (similar to the color change due to wetting, when water is supplied
562 to the soil specimen that is initially relatively dry), as a result of pore water freezing to ice or
563 vice versa. Liu et al. (2018) suggested that the grey value change should be considered when
564 using PIV to quantify frozen soil deformation. However, this problem seems not have
565 significant influence on the PIV calculation in the present study. In addition, fog is likely to
566 form on the transparent acrylic wall, whose temperature is lower than that of ambient air. This
567 will significantly affect the quality of soil images (e.g., Dagli et al., 2018 and the present study).
568 In the studies by McKnight-Whitford (2013) and Wang et al. (2020), an antifogging agent and
569 a deicer were sprayed on the outside of the glass window before testing. Furthermore, no
570 apparent ice lenses were observed in the present study, which facilitated the use of PIV. In the
571 case that ice lenses form during the freezing process, large subset size (which is significantly
572 larger than the thickness of the ice lens such that it involves both the ice lens and enough soil
573 texture) may be employed to achieve reasonable PIV result.

574 In the present study, the whole frost heave setup was placed in a large environmental
575 chamber. In this case, accurate temperature boundary conditions can be exerted on the four
576 sides of the soil tank model. More importantly, the constant lighting condition and large space
577 in this environmental chamber facilitated the establishment of accurate PIV analysis, without
578 modifying the frost heave test setup. For example, in the study by Dagli et al. (2018), an opening
579 has been made to the insulation material of the frost heave test cell in order to capture the images

of the freezing specimen. This method inevitably introduced disturbance to the boundary conditions of the frost heave test.

The PIV technique is particularly useful for quantifying the thaw settlement of the soil specimen. This is because the friction between the top plate and acrylic wall prevented the free downward movement of the top plate. As the LVDT was mounted on the top plate, it is apparent that it could not measure the real thaw settlement of the soil specimen. This issue can be further supported by the observed gap between the top plate and thawed specimen. On the other hand, the friction might have also contributed to mitigating the frost heave during the freezing process. However, the magnitude of the friction or its effect on the frost heave of the soil specimen could not be quantified. For future studies, installing earth pressure cell on the top surface of the soil specimen may give more insights into this issue.

6. Summary

The freezing of water to form ice is one of the most common phase transformations in the natural environment (Wettlaufer, 1999). The increasing use of the seasonally frozen and permafrost regions for civil engineering constructions and the effects of global warming on these regions have stimulated research on the behaviors of frozen soils. Among the behaviors of frozen soils, frost heave induced by water and vapor transfer in the soil mass has been the research topic for decades.

In the present study, the frost heave characteristics of the Komaoka soil, which is a typical soil with volcanic nature found in the Hokkaido prefecture of Japan was investigated. A relatively large soil tank model was established in laboratory for this purpose. The effects of temperature boundary, external water supply, and water transfer type on the frost heave characteristics of the Komaoka soil were studied, through a series of frost heave tests. In addition to the frost heave measured by a displacement sensor, the PIV technique was used to quantify the full field deformation of the soil specimen. Discussions regarding the presented experimental investigation and the employment of PIV technique for computing frozen soil deformation are summarized.

The results suggest that temperature gradient inside the soil specimen is the driving force for the migration of pore water and vapor. The largest increment in water content generally

agrees well with the frost penetration depth. The contribution of vapor to the frost heave of the Komaoka soil specimen is typically small under the present testing conditions. The seeding method, selected subset size, control points setup, and calculation processes ensured accurate PIV results. These findings can provide valuable insights into the frost heave behavior of the Komaoka soil in particular, as well as into the application of PIV for frozen soil engineering in general.

Acknowledgement

The study is supported by the Fundamental Research Funds for the Central Universities (lzujbky-2021-kb03, lzujbky-2021-sp67), and the Open Fund from the State Key Laboratory of Frozen Soil Engineering, Chinese Academy of Sciences (CAS) (SKLFSE202102). The first author also gratefully acknowledges the financial support from the Japan Society for the Promotion of Science (JSPS).

References

Arenson, L. U., Sego, D. C., and Take, W. A. 2007. Measurement of ice lens growth and soil consolidation during frost penetration using particle image velocimetry (PIV). In 60th Canadian Geotechnical Conference, Ottawa, ON (pp. 2046-2053).

Azmatch, T.F., Arenson, L.U., Sego, D.C. and Biggar, K.W., 2008. Measuring ice lens growth and development of soil strains during frost penetration using particle image velocimetry (GeoPIV). In Proceedings of the Ninth International Conference on Permafrost, Fairbanks, Alaska (Vol. 1, pp. 89-93).

Bhandari, A.R., Powrie, W. and Harkness, R.M., 2012. A digital image-based deformation measurement system for triaxial tests. Geotechnical Testing Journal, 35(2), pp.209-226.

Dagli, D., Zeinali, A., Gren, P., and Laue, J. 2018. Image analyses of frost heave mechanisms based on freezing tests with free access to water. Cold Regions Science and Technology, 146, 187-198.

Gao, Q., Lin, H., Tu, H., Zhu, H., Wei, R., Zhang, G., and Shao, X. 2021. A robust single-pixel particle image velocimetry based on fully convolutional networks with cross-correlation embedded. Physics of Fluids, 33(12), 127125.

Gao, Z., Lin, Z., Niu, F., and Luo, J. 2020. Soil water dynamics in the active layers under different land-cover types in the permafrost regions of the Qinghai–Tibet Plateau, China. Geoderma, 364, 114176.

He, H., Flerchinger, G. N., Kojima, Y., Dyck, M., and Lv, J. 2021. A review and evaluation of 39 thermal conductivity models for frozen soils. Geoderma, 382, 114694.

Kawamura, S. and Miura, S., 2013. Rainfall-induced failures of volcanic slopes subjected to freezing and thawing. Soils and Foundations, 53(3), pp.443-461.

Konrad, J.M., 1988. Influence of freezing mode on frost heave characteristics. Cold Regions Science and Technology, 15(2), pp.161-175.

Liu, J., Yuan, B., and Dimaano, R. 2011. Optical measurement of sand deformation around a laterally loaded pile. Journal of Testing and Evaluation, 39(5), 754-759.

Liu, Z. Y., Liu, J. K., Li, X., Hu, T., and Fang, J. 2018. Application of PIV in model tests on frozen unsaturated soils and grayscale correlation analysis. Chinese Journal of Geotechnical Engineering, 40(2), 313-320. (in Chinese)

Lu, N., Likos, W. J., Luo, S., and Oh, H. 2021. Is the Conventional Pore Water Pressure Concept Adequate for Fine-Grained Soils in Geotechnical and Geoenvironmental Engineering?. Journal of Geotechnical and Geoenvironmental Engineering, 147(10), 02521001.

McKnight-Whitford, H. 2013. Development of an experimental device for monitoring frost heave in soils. Master thesis, Dalhousie University, Halifax, Nova Scotia, Canada.

Neall, V.E., 2009. Volcanic soils. Land use, land cover and soil sciences, 7, pp.23-45.

Nguyen, T.B., 2017. Effect evaluation of grass on infiltration and seepage of volcanic soil ground. Master thesis, Hokkaido University, Sapporo, Japan.

Nishimura, S., Iwaki, A., Takashino, S. and Tanaka, H., 2016. Image-based measurement of one-dimensional compressibility in cement-treated soils. Géotechnique, 66(10), pp.840-853.

Nishimura, S., Okajima, S., Joshi, B. R., Higo, Y., and Tokoro, T. 2021. Volumetric behaviour of clays under freeze–thaw cycles in a mesoscopically uniform element. Géotechnique, 71(12), 1150-1164.

Peppin, S. S., and Style, R. W. 2013. The physics of frost heave and ice-lens growth. Vadose Zone Journal, 12(1).

Rempel, A. W. 2010. Frost heave. Journal of Glaciology, 56(200), 1122-1128.

Ren, J., Zhang, S., Wang, C., Ishikawa, T., and Vanapalli, S. K. 2021. The Measurement of Unfrozen Water Content and SFCC of a Coarse-Grained Volcanic Soil. Journal of Testing and Evaluation, 51(1).

Saberi, P. S., and Meschke, G. 2021. A hysteresis model for the unfrozen liquid content in freezing porous media. Computers and Geotechnics, 134, 104048.

Smith, M.W., 1985. Models of soil freezing. In Field and Theory: Lectures in Geocryology, edited by Church, M. and Slaymaker, O., Vancouver: Univ. of British Columbia Press, pp. 96-120.

Stanier, S.A., Blaber, J., Take, W.A. and White, D.J., 2016a. Improved image-based deformation measurement for geotechnical applications. Canadian Geotechnical Journal, 53(5), pp.727-739.

Stanier, S., Dijkstra, J., Leśniewska, D., Hambleton, J., White, D. and Wood, D.M., 2016b. Vermiculate artefacts in image analysis of granular materials. Computers and Geotechnics, 72, pp.100-113.

Stanier, S.A. and White, D.J., 2013. Improved image-based deformation measurement in the centrifuge environment. Geotechnical Testing Journal, 36(6), pp.915-928.

Sweidan, A. H., Niggemann, K., Heider, Y., Ziegler, M., and Markert, B. 2022. Experimental study and numerical modeling of the thermo-hydro-mechanical processes in soil freezing with different frost penetration directions. Acta Geotechnica, 17(1), 231-255.

Take, W. A. 2015. Thirty-Sixth Canadian Geotechnical Colloquium: Advances in visualization of geotechnical processes through digital image correlation. Canadian Geotechnical Journal, 52(9), 1199-1220.

Teng, J., Shan, F., He, Z., Zhang, S., Zhao, G. and Sheng, D., 2019. Experimental study of ice accumulation in unsaturated clean sand. Géotechnique, 69(3), pp.251-259.

Viggiani, G., and Hall, S. A. 2012. Full-field measurements in experimental geomechanics: historical perspective, current trends and recent results. ALERT Doctoral School, 3-68.

690 Wang, M., Li, X., Liu, Z., Liu, J. and Chang, D., 2020. Application of PIV Technique in Model Test of
691 Frost Heave of Unsaturated Soil. Journal of Cold Regions Engineering, 34(3), p.04020014.
692 Wang, T.L., Zhang, Y.Z., Wei, M., Cheng, B.Y. and Wen, A., 2019. Investigation of liquid and vapor
693 migration in coarse-grained soil during open-system step-freezing test. Cold Regions Science and
694 Technology, 165, p.102816.
695 Watanabe, K., 1999. Ice lensing mechanism during soil freezing. Doctoral thesis, Mie University, Japan.
696 Wettlaufer, J. S. 1999. Ice surfaces: macroscopic effects of microscopic structure. Philosophical
697 Transactions of the Royal Society of London. Series A: Mathematical, Physical and Engineering
698 Sciences, 357(1763), 3403-3425.
699 White, D.J., Take, W.A. and Bolton, M.D., 2003. Soil deformation measurement using particle image
700 velocimetry (PIV) and photogrammetry. Geotechnique, 53(7), pp.619-631.
701 White, D. J., Take, W. A., and Bolton, M. D. 2005. Discussion of "Accuracy of digital image correlation
702 for measuring deformations in transparent media" by Samer Sadek, Magued G. Iskander, and
703 Jinyuan Liu. Journal of computing in civil engineering, 19(2), 217-219.
704 White, D. J., Take, W. A., Bolton, M. D., and Munachen, S. E. 2001. A deformation measurement
705 system for geotechnical testing based on digital imaging, close-range photogrammetry, and PIV
706 image analysis. In Proceedings of the 15th International conference on soil mechanics and
707 geotechnical engineering (Vol. 1, pp. 539-542). AA Balkema Publishers.
708 Williams, P.J. and Smith, M.W., 1989. The frozen earth: fundamentals of geocryology. Cambridge
709 University Press.
710 Xu, J., Wu, Z., Chen, H., Shao, L., Zhou, X., and Wang, S. 2021. Triaxial shear behavior of basalt fiber-
711 reinforced loess based on digital image technology. KSCE Journal of Civil Engineering, 25(10),
712 3714-3726.
713 Xu, J., Wu, Z., Chen, H., Shao, L., Zhou, X., and Wang, S. 2022. Influence of dry-wet cycles on the
714 strength behavior of basalt-fiber reinforced loess. Engineering Geology, 302, 106645.
715 Yin, X., Liu, E., Song, B., and Zhang, D. 2018. Numerical analysis of coupled liquid water, vapor, stress
716 and heat transport in unsaturated freezing soil. Cold Regions Science and Technology, 155, 20-28.
717 Zeinali, A., Edeskär, T., and Laue, J. 2020. Mechanism of thawing. Cogent Engineering, 7(1), 1716438.
718 Zhang, S., Teng, J., He, Z. and Sheng, D., 2016. Importance of vapor flow in unsaturated freezing soil:
719 a numerical study. Cold Regions Science and Technology, 126, pp.1-9.
720 Zhou, J., Wei, C., Wei, H., and Tan, L. 2014. Experimental and theoretical characterization of frost
721 heave and ice lenses. Cold regions science and technology, 104, 76-87.

Table 1. Physical properties of the Komaoka soil

G_s	ρ_{dmax} (g/cm^3)	ρ_{dmin} (g/cm^3)	w_0 (%)	ρ_d (g/cm^3)	w_{hygro} (%)	%Sand	%Silt	%Clay	C_u	C_c
2.50	1.12	0.76	≈ 30	0.915	0.96	64	28	8	45	1.54

Note: G_s: specific gravity; ρ_{dmax} and ρ_{dmin}: the maximum and minimum dry density, respectively; w_0: the natural gravimetric water content; ρ_d: dry density; w_{hygro}: hygroscopic water content; C_u: coefficient of uniformity; C_c: coefficient of curvature. Values for G_s, ρ_{dmax} and ρ_{dmin} are from Kawamura and Miura (2013); value for w_0 is from Nguyen (2017).

Table 2. Summary of the eight frost heave tests

ID	Initial w%	Open- or Closed-system	Coarse layer	Seeding	Freezing			Thawing		
					Top (ºC)	Bottom (ºC)	Side (ºC)	Top (ºC)	Bottom (ºC)	Side (ºC)
Test 1	30	Closed	No	No	-10	20	5	NA		
Test 2	15	Closed	No	No	-10	20		25	20	RT
Test 3	30	Closed	No	Yes	-15	15		25	15	
Test 5	30	Open	No	Yes	-15	15		25	15	
Test 4	10	Open	Komaoka soil (2.8 - 9.5mm)	Yes	-10	20		25	20	
Test 6	15	Open	Glass beads (2.0 - 4.0mm)	Yes	-10	20		25	20	
Test 7	7	Open	Glass beads (2.0 - 4.0mm)	Yes	-10	20		25	20	
Test 8	7	Open	Glass beads (2.0 - 4.0mm)	Yes	-20	10		25	10	

Note: w%: gravimetric water content; RT: room temperature, around 22ºC; Top/Bottom: the controlled temperature of the Top/Bottom plate; Side: the controlled temperature of the environmental chamber. The dry density of the soil specimen was controlled to 0.915g/cm^3 throughout this study. NA: not applicable.

List of Figures

Fig. 1. The location of the sampling site

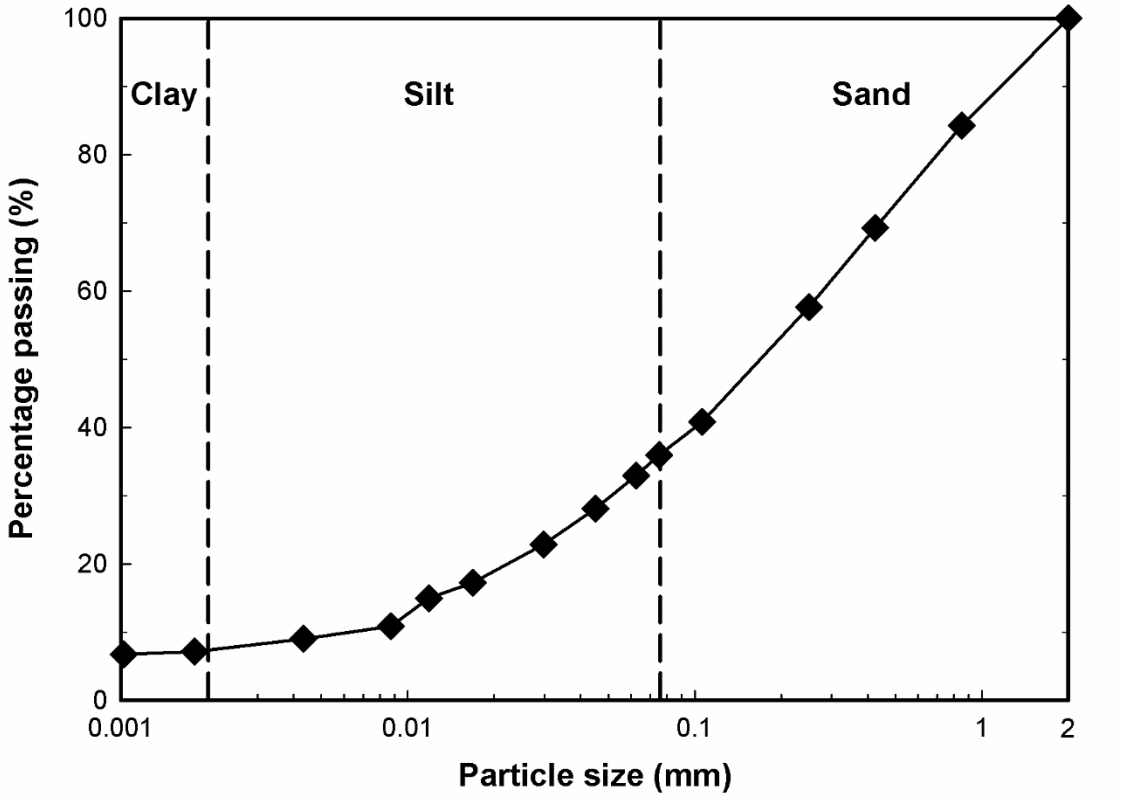

Fig. 2. The gradation curve of the Komaoka soil used for frost heave test

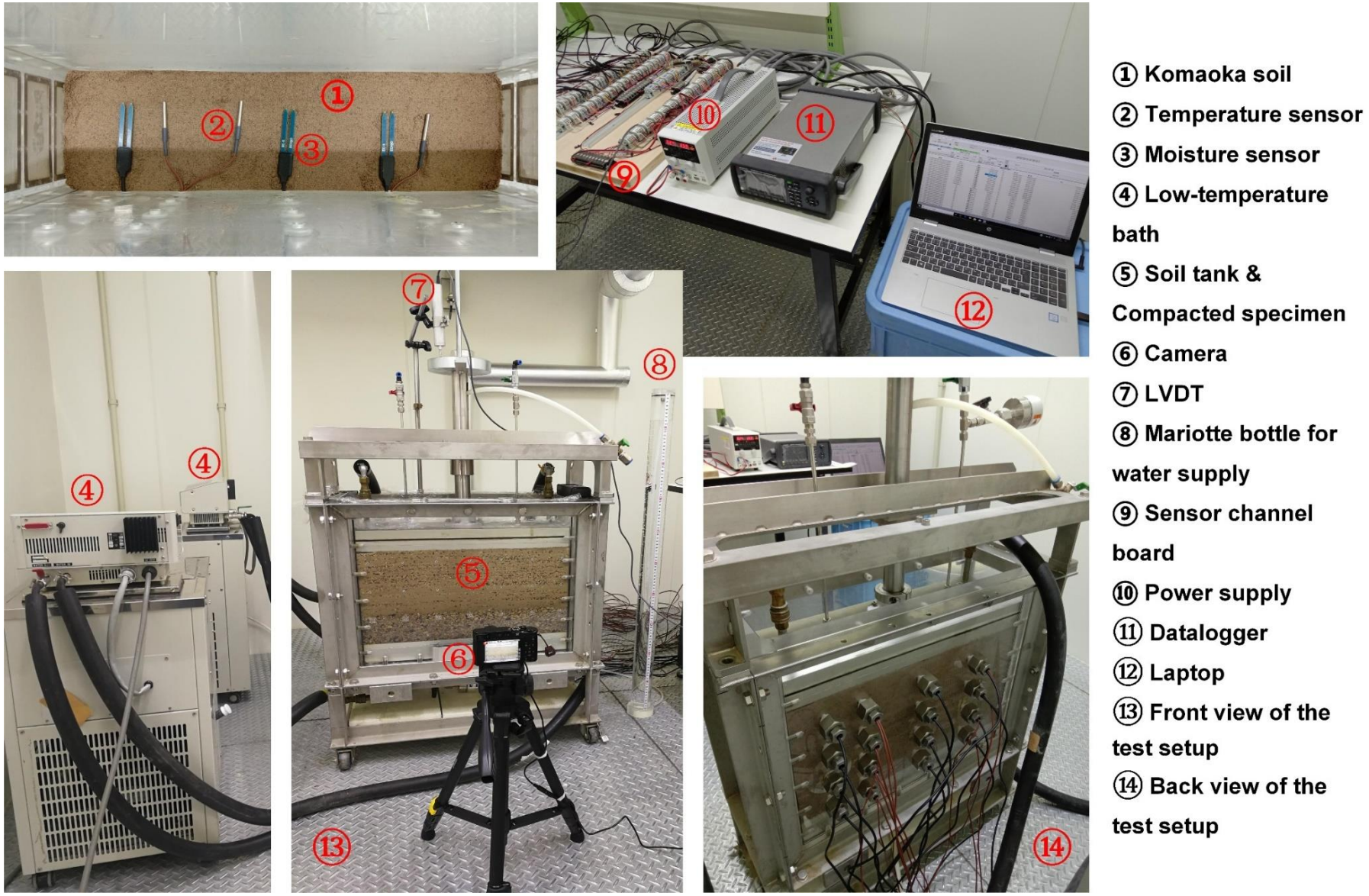

Fig. 3. The setup of the frost heave test

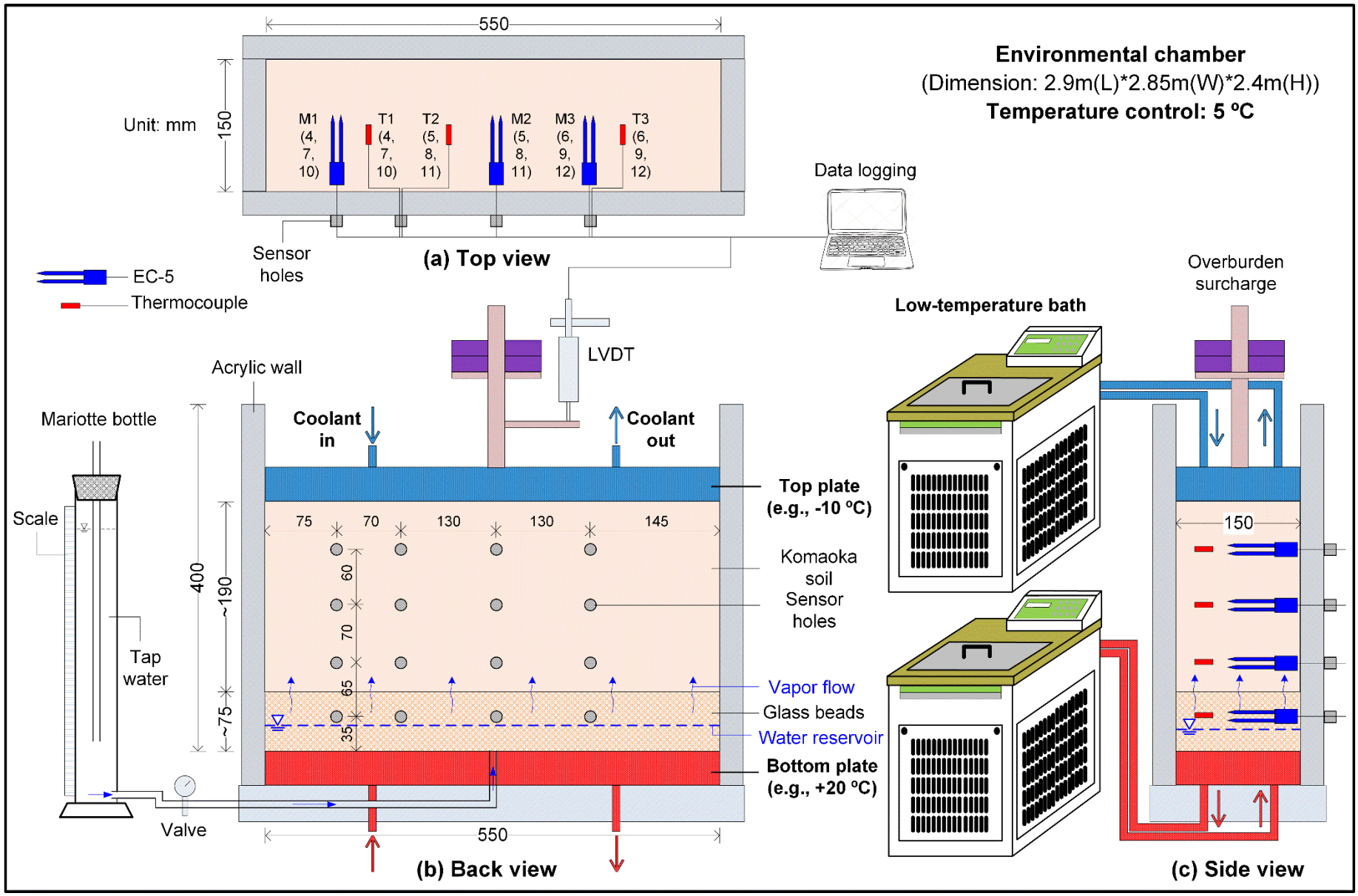

Fig. 4. The schematic diagram of the frost heave test

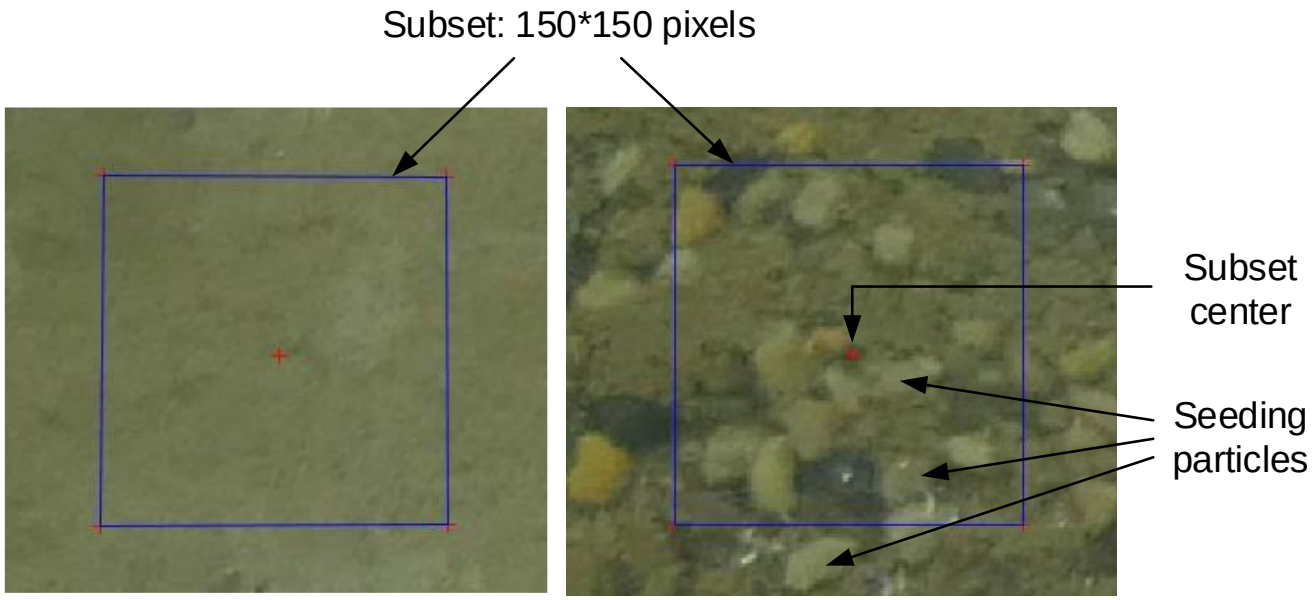

Fig. 5. Comparison between (a) Test 2: without seeding and (b) Test 5: with seeding

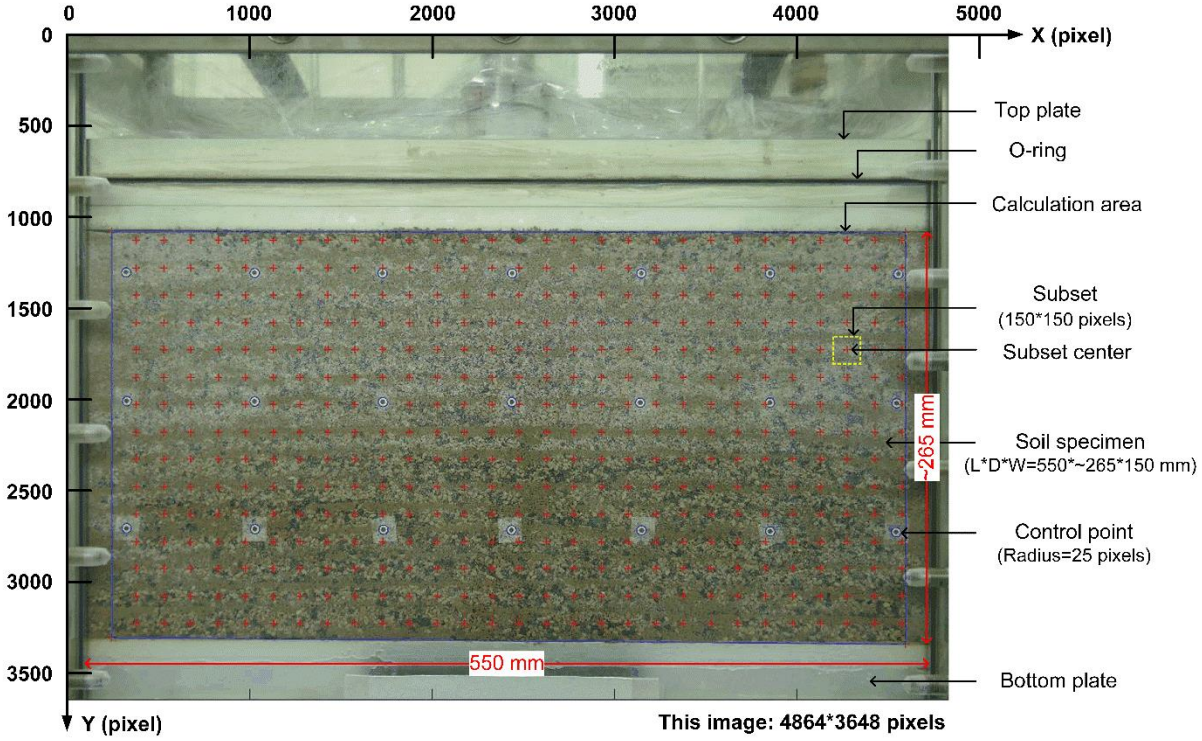

Fig. 6. The generated subsets for Test 5

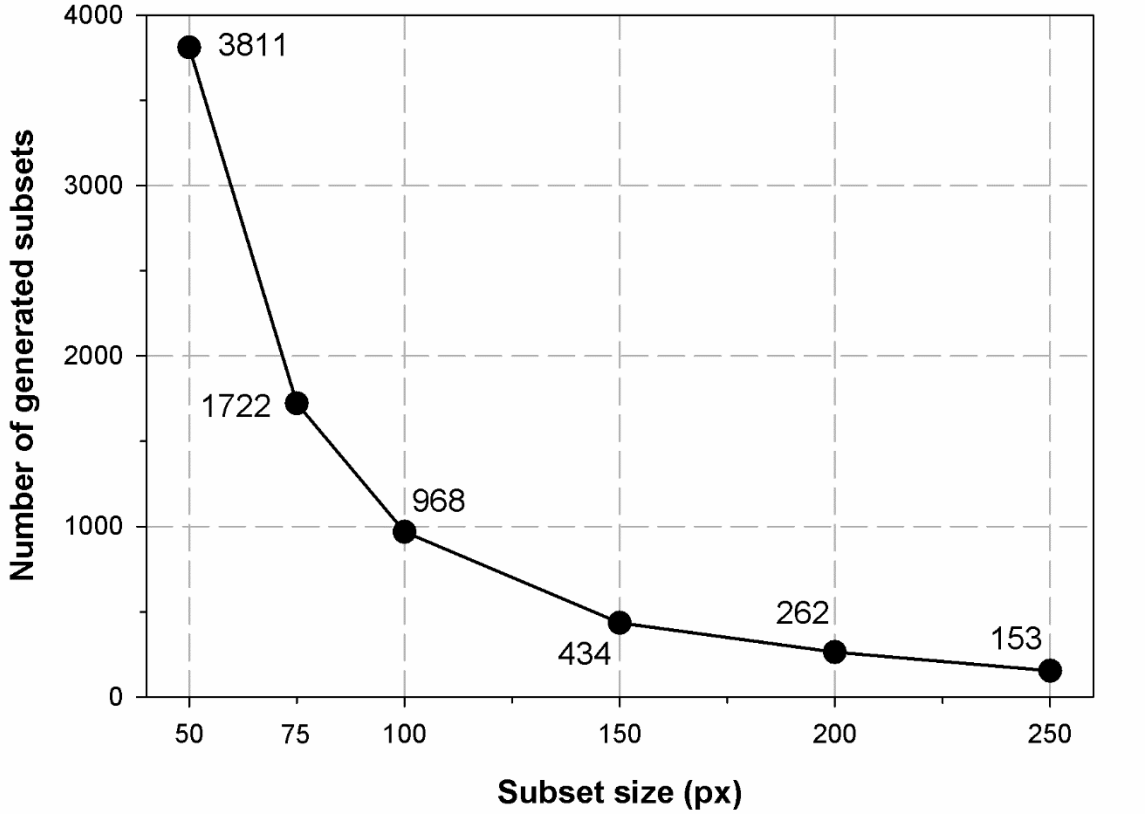

Fig. 7. The effect of subset size on the number of generated subsets for Test 5

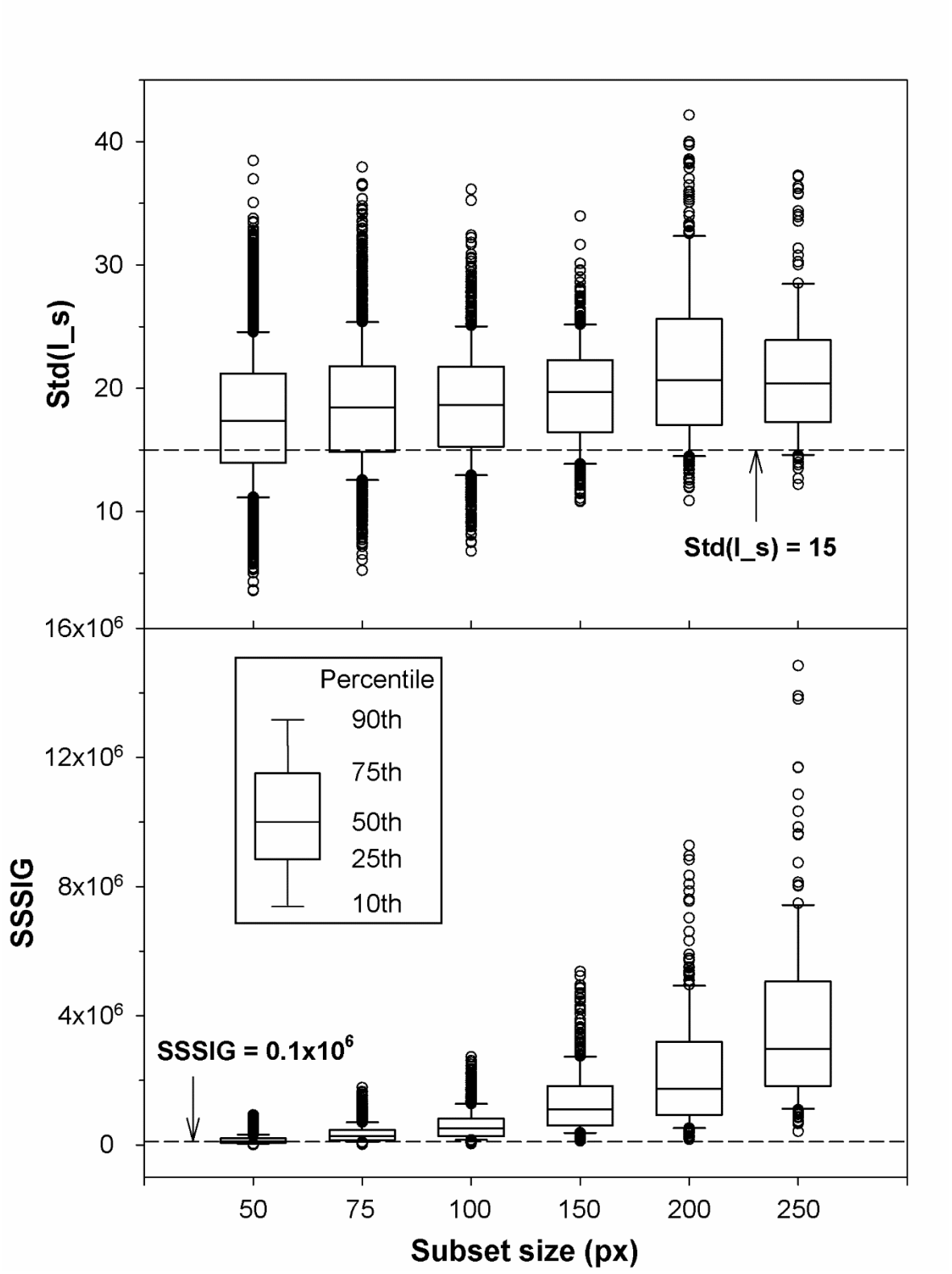

Fig. 8. The effect of subset size on the Std(I_s) and SSSIG of the generated subsets for Test 5

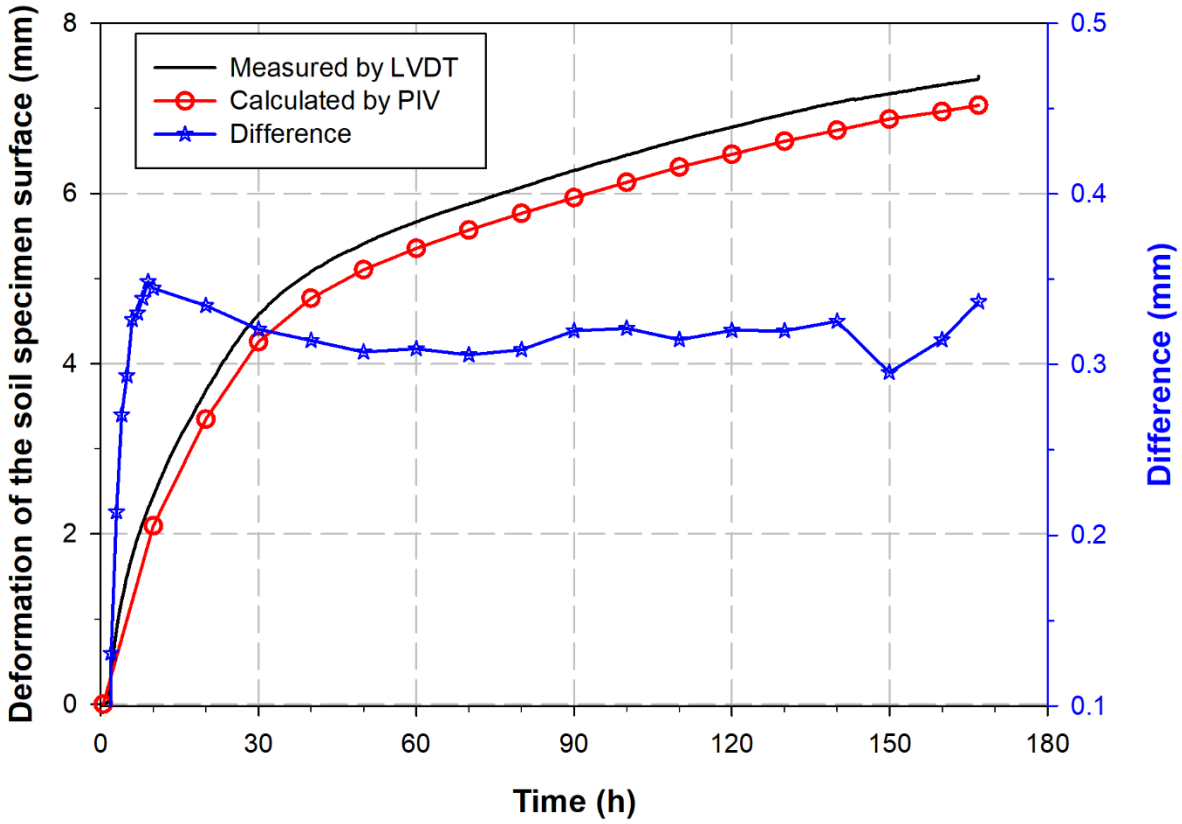

Fig. 9. Comparison between the vertical displacement of soil specimen obtained by PIV and LVDT for Test 5 (PIV subset size: 150 pixels)

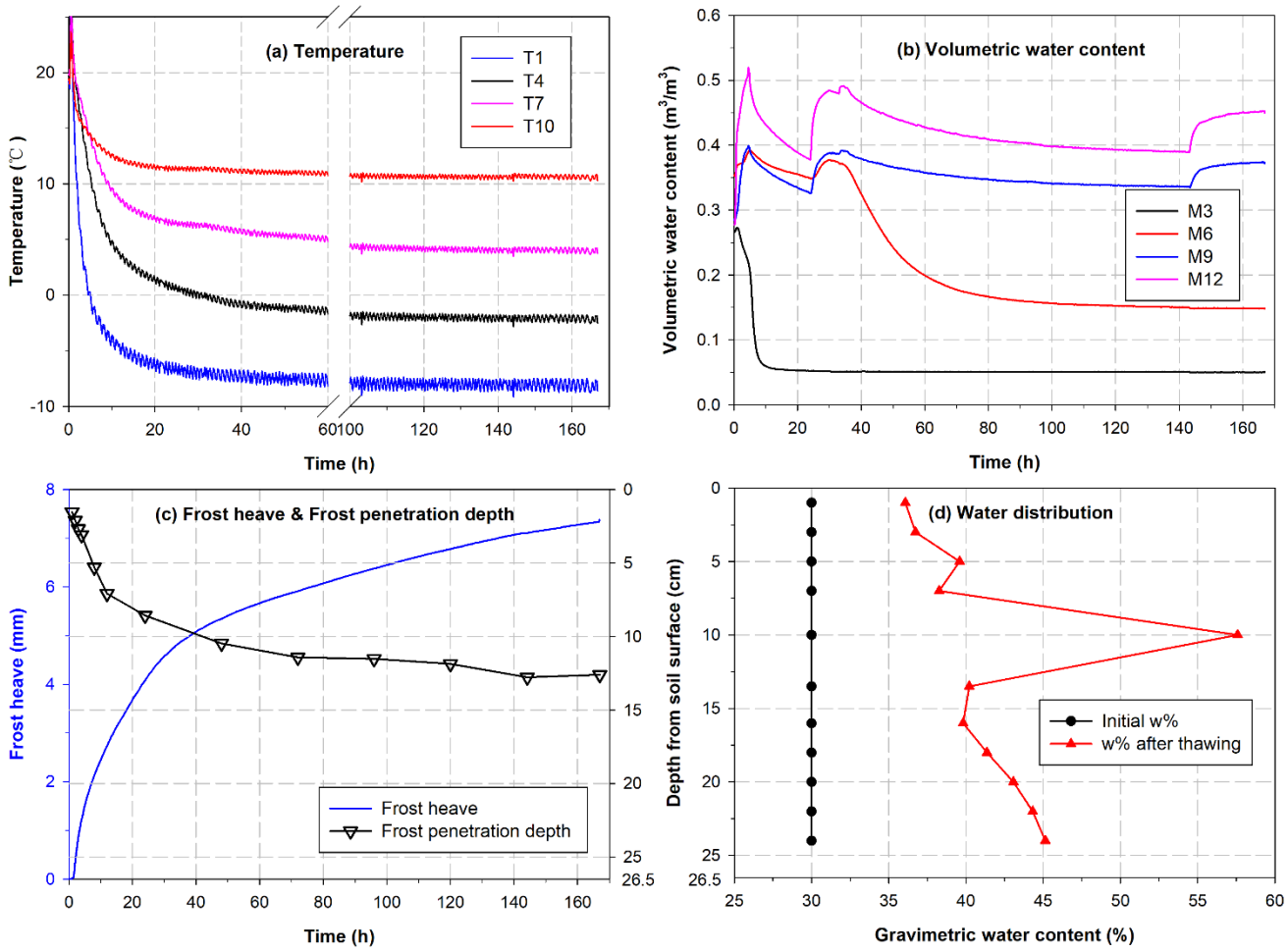

Fig. 10. The experimental results of Test 5: (a) temperature variation, (b) volumetric water content variation, (c) frost heave and frost penetration depth, and (d) water distribution

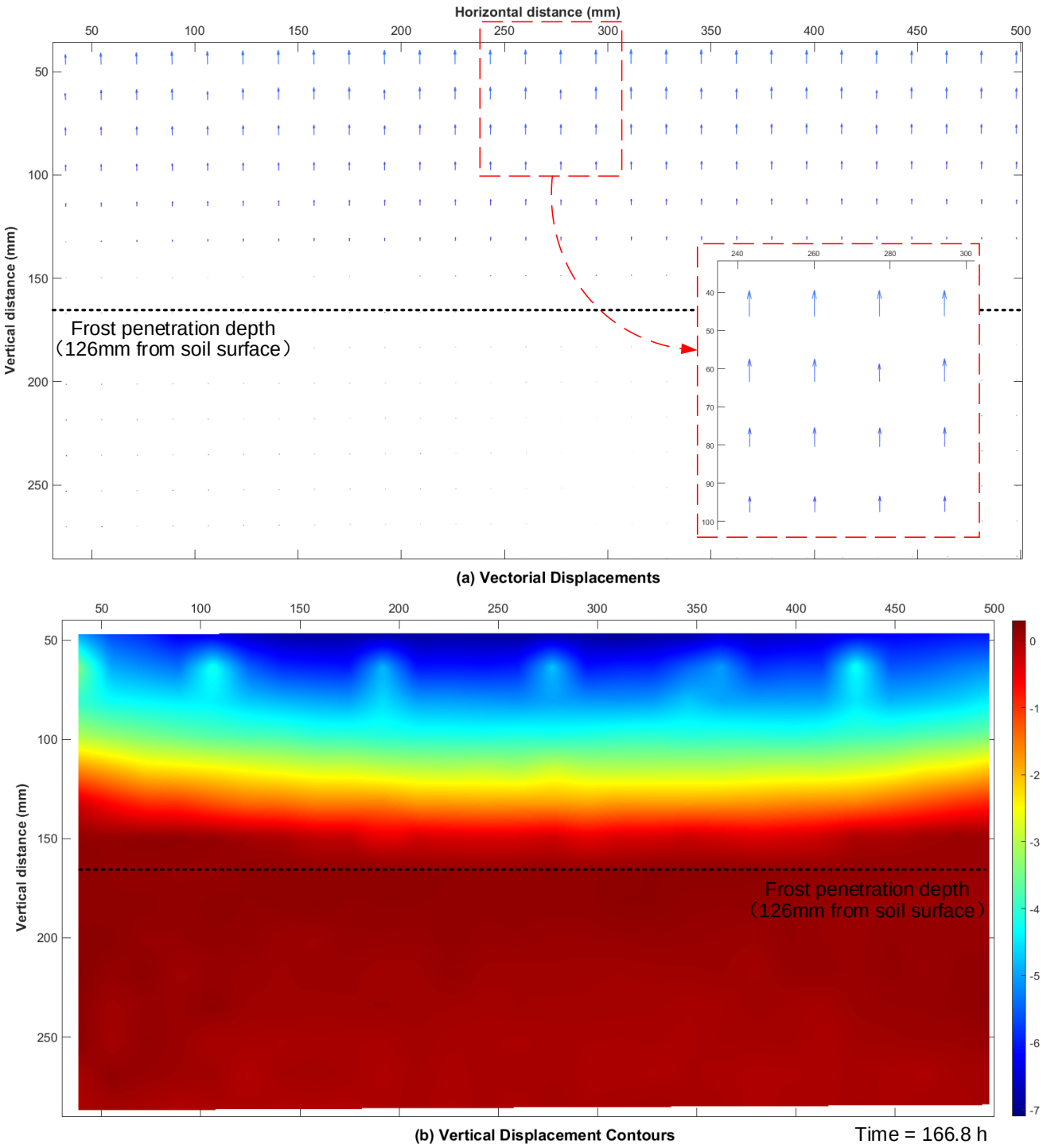

Fig. 11. The (a) vectorial displacements and (b) vertical displacement contours of the soil specimen in Test 5 when the maximum frost heave was achieved (PIV subset size: 150 pixels)

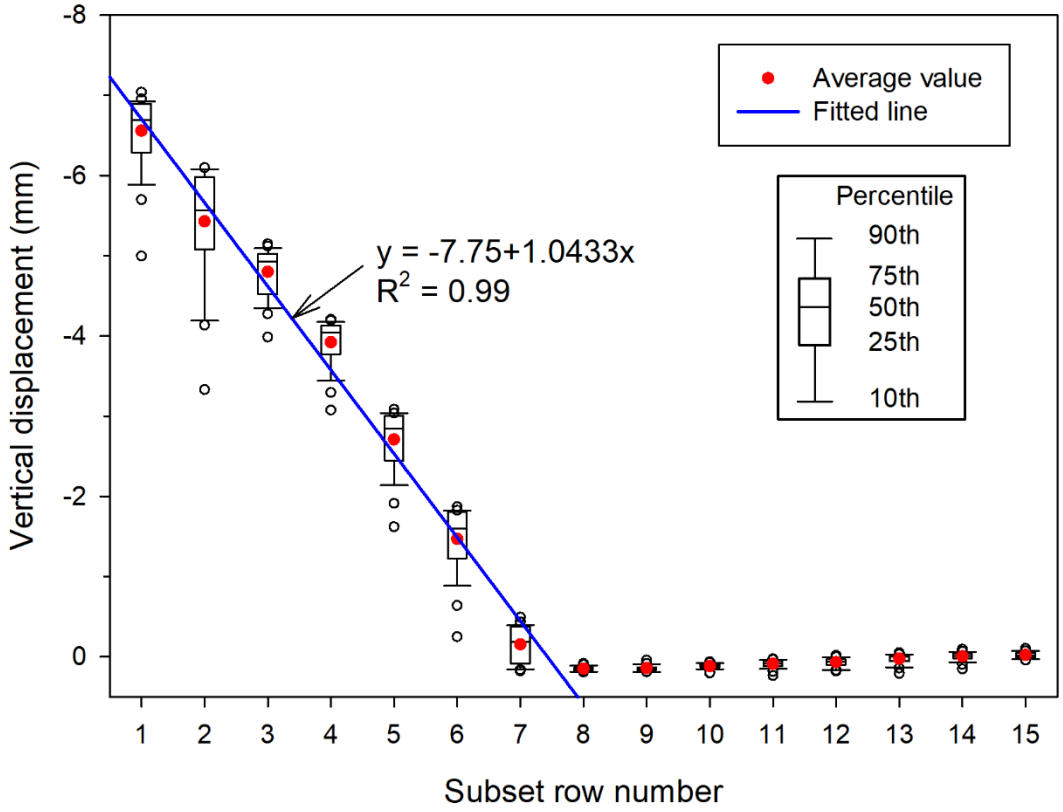

Fig. 12. The linear distribution of vertical displacement of the soil specimen in Test 5 (PIV subset size: 150 pixels)

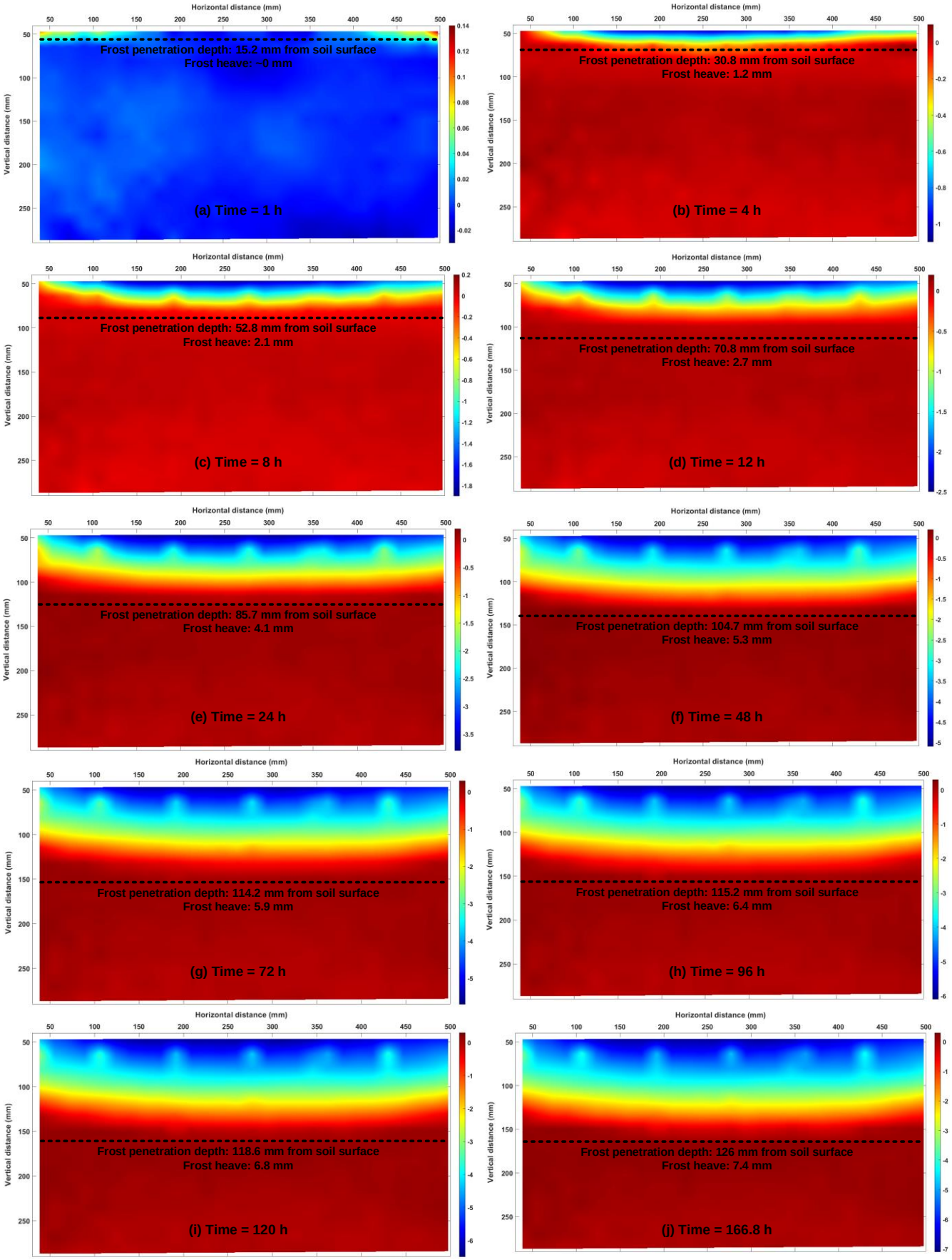

Fig. 13. The vertical displacement contours of the soil specimen in Test 5 at different times (PIV subset size: 150 pixels)

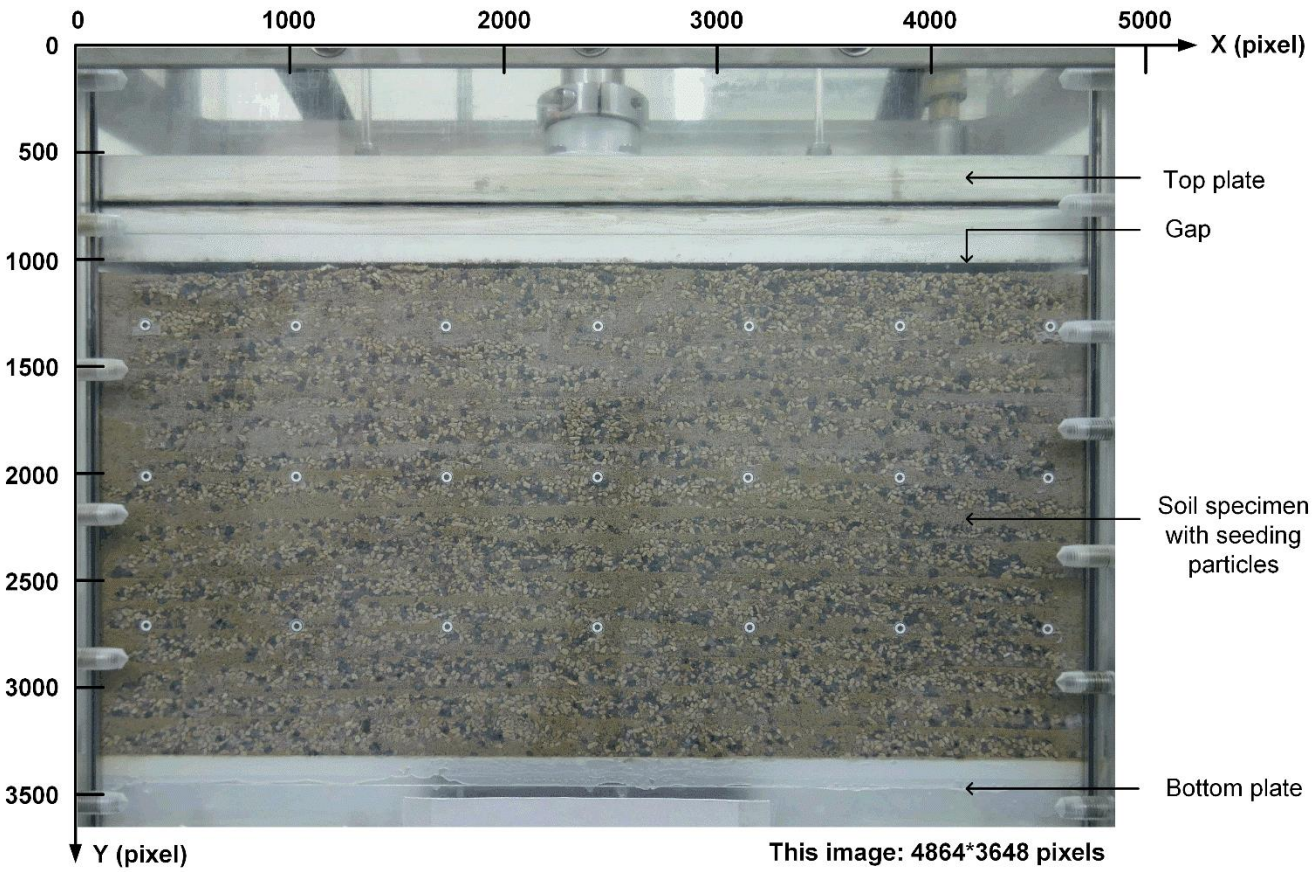

Fig. 14. The gap between the top plate and thawed soil specimen

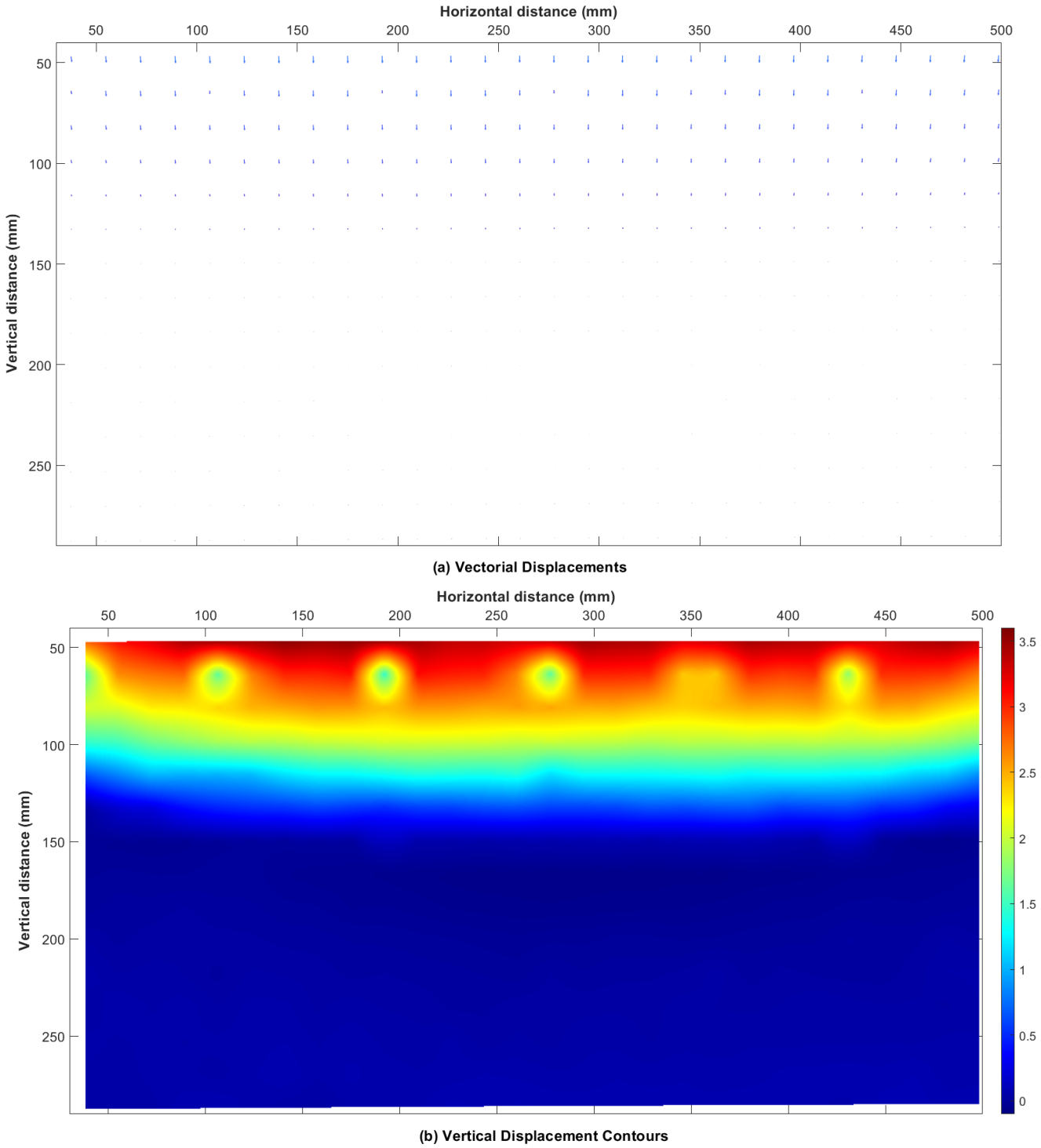

Fig. 15. The (a) vectorial displacements and (b) vertical displacement contours of the soil specimen after thawed in Test 5 (PIV subset size: 150 pixels)

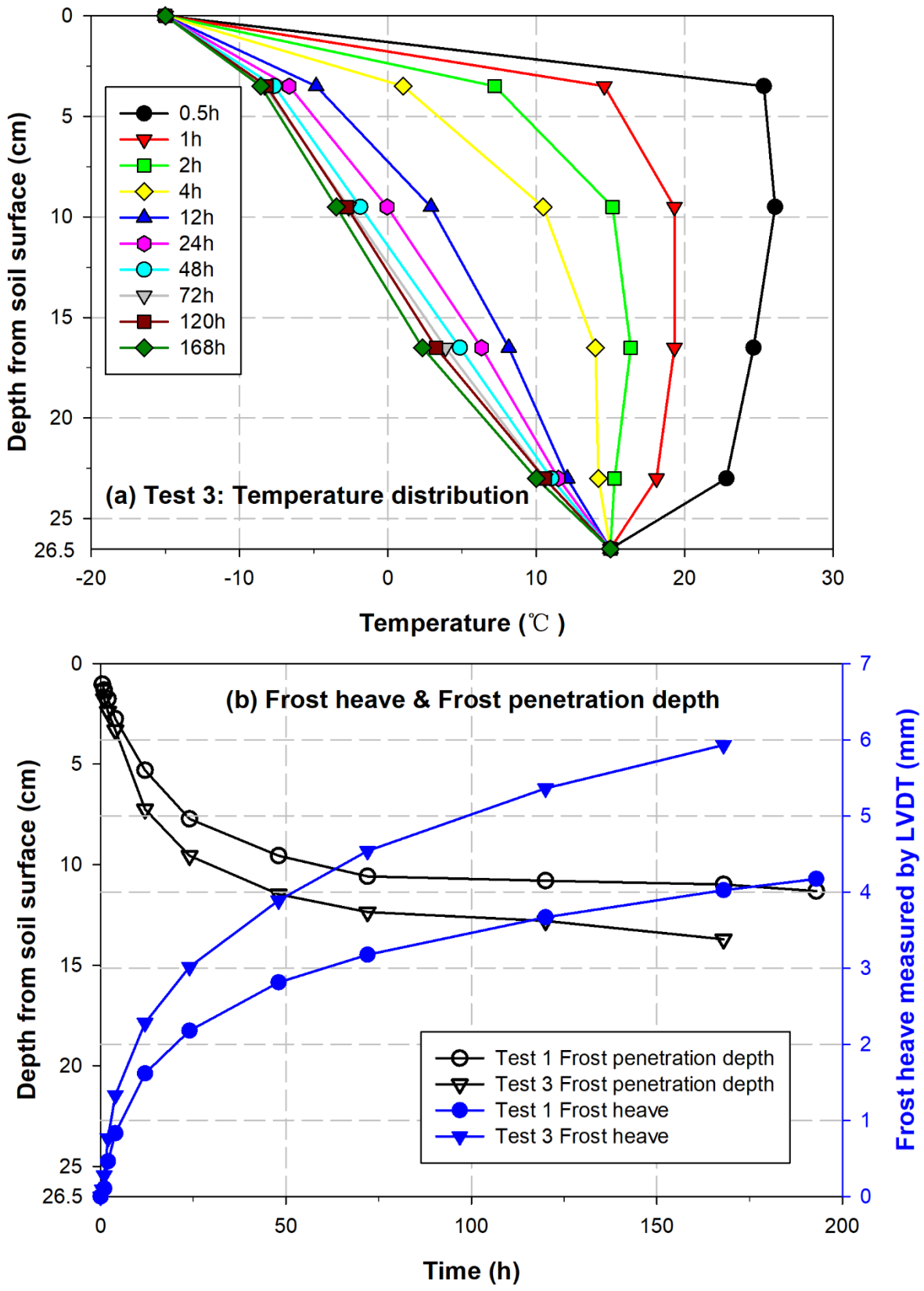

Fig. 16. The (a) temperature distribution curve of Test 3 and (b) comparison between Test 1 and Test 3

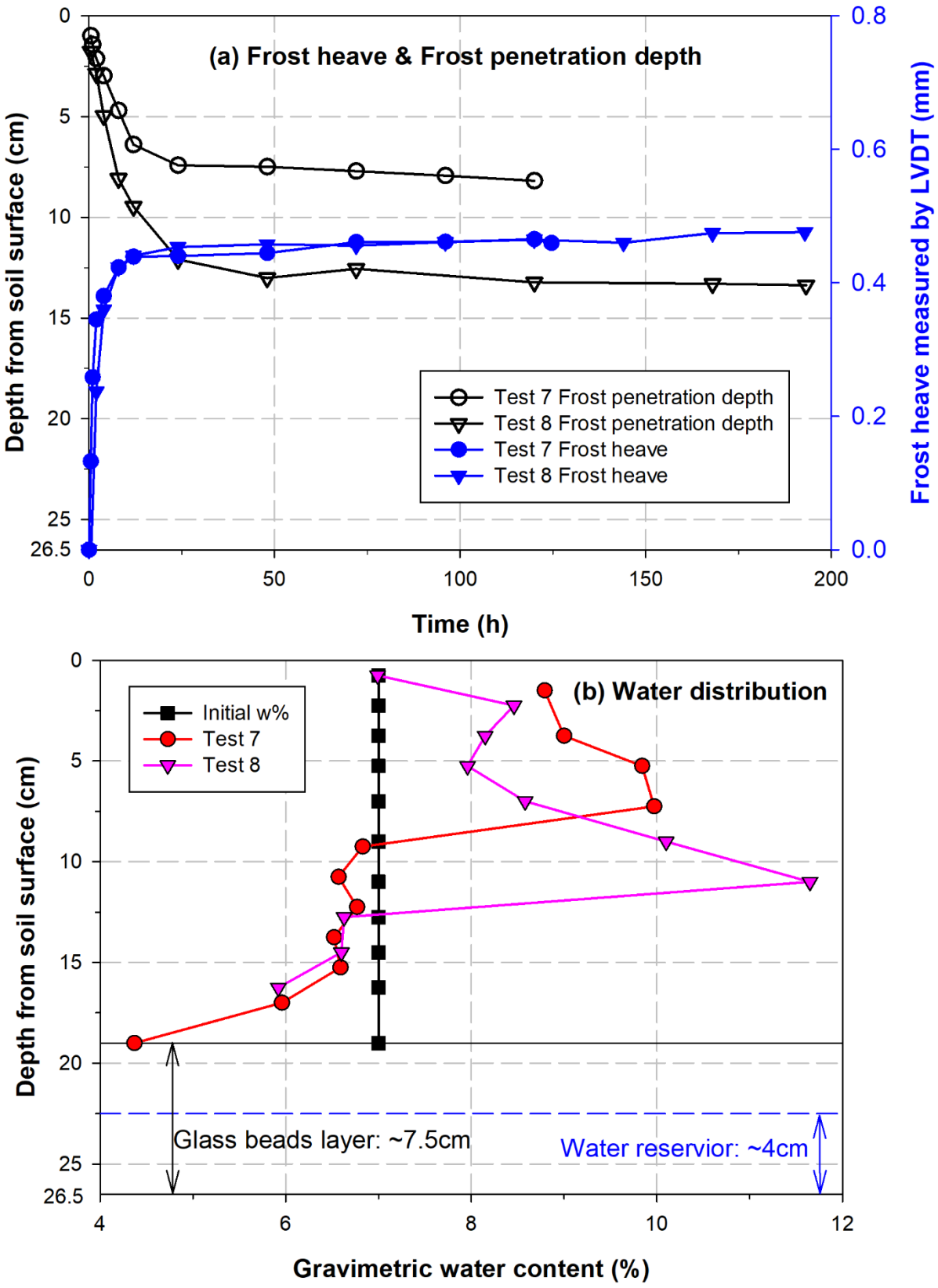

Fig. 17. The comparison between Test 7 and Test 8: (a) frost heave and frost penetration depth and (b) water distribution

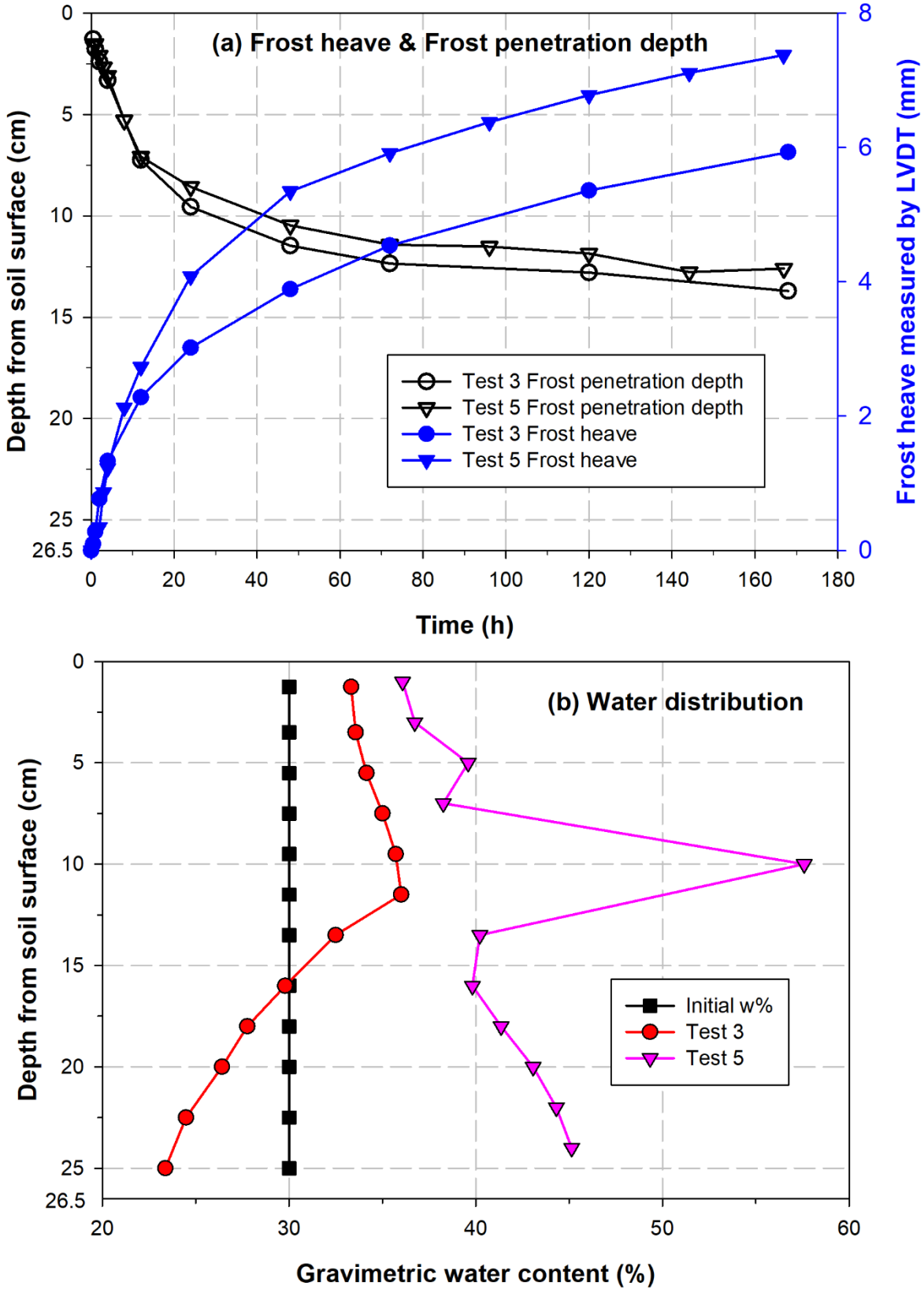

Fig. 18. The comparison between Test 3 and Test 5: (a) frost heave and frost penetration depth and (b) water distribution

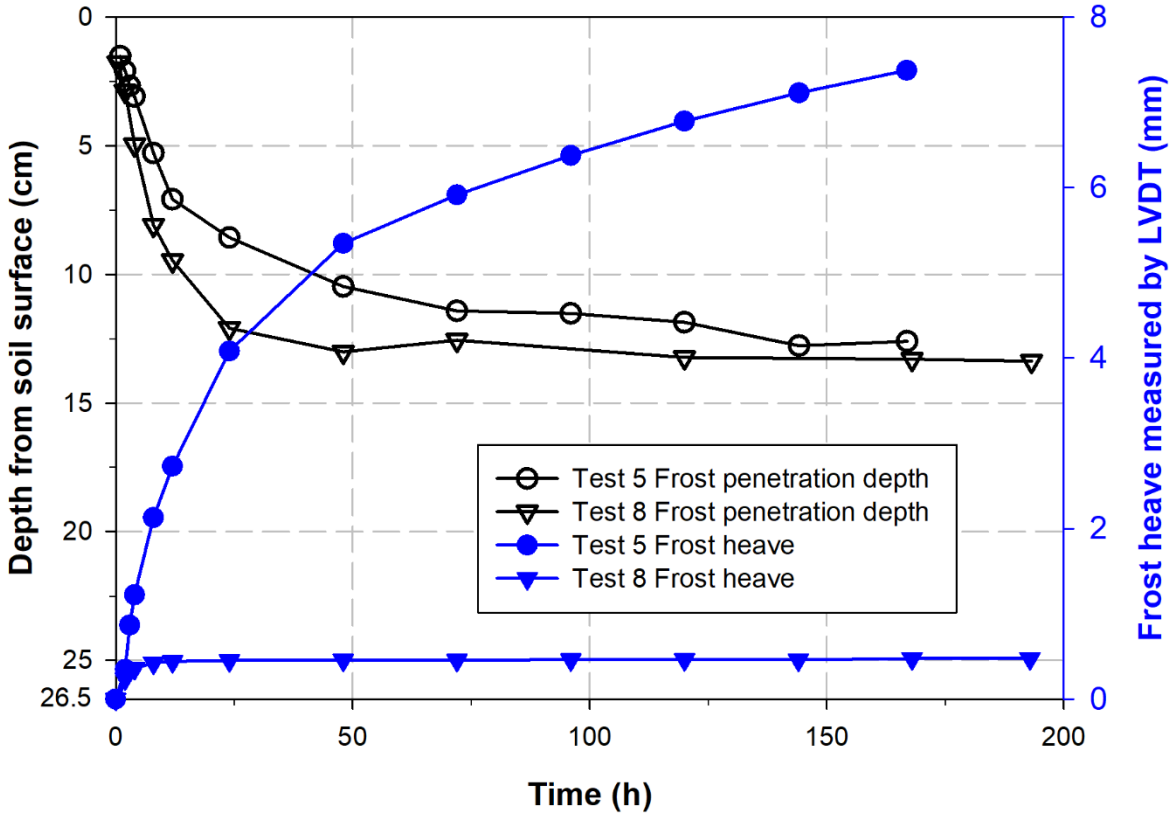

Fig. 19. The comparison between Test 5 and Test 8

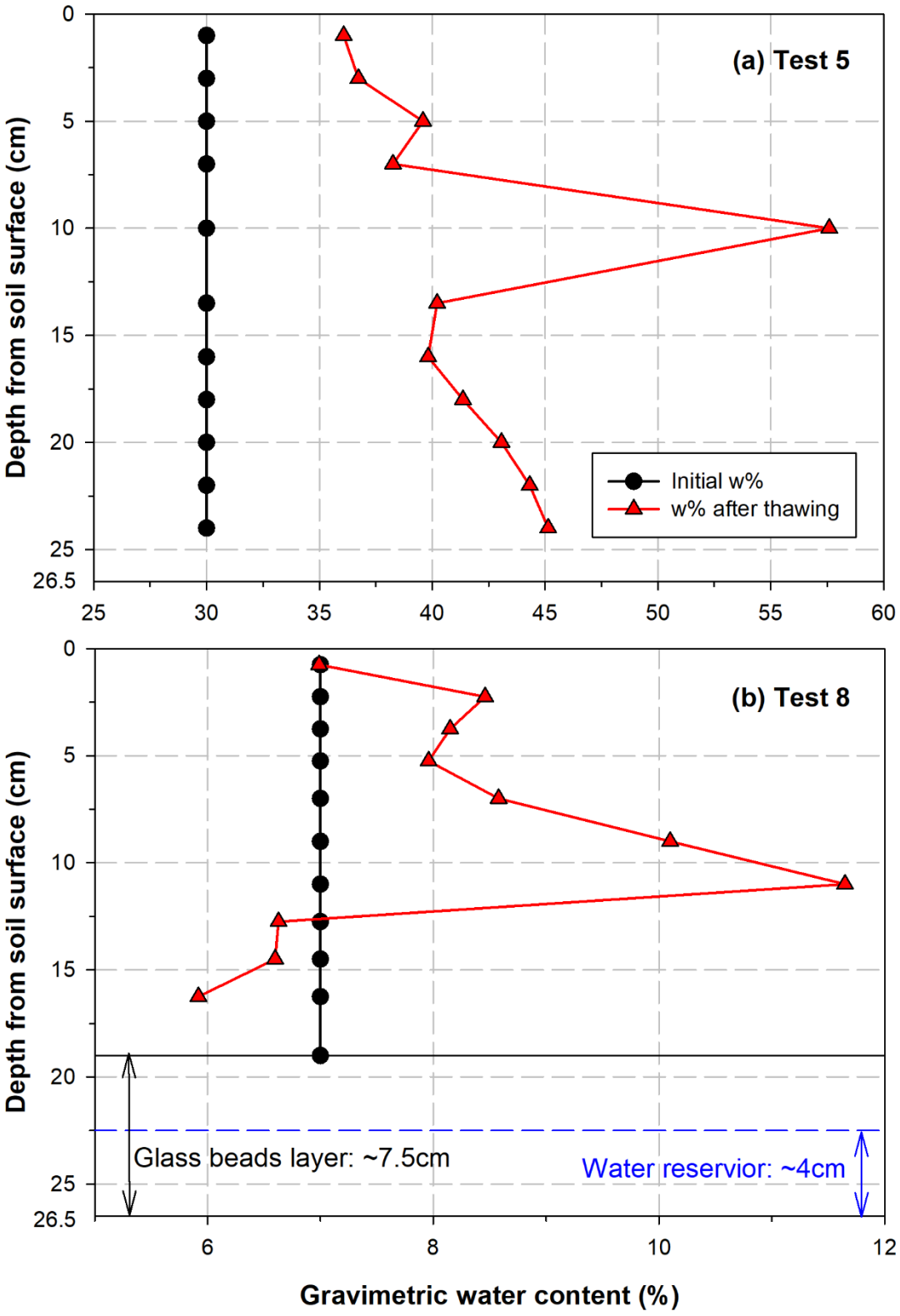

Fig. 20. Water distribution in the soil specimen of (a) Test 5 and (b) Test 8